Mathematisch-Naturwissenschaftliche Fakultät
Ernst-Moritz-Arndt-Universität Greifswald

Master Thesis

Physics of Ion Thrusters' Plumes

Karl Felix Lüskow
Greifswald, July 10, 2013

Referees:
Prof. Dr. Ralf Schneider
Prof. Dr. Jürgen Meichsner

Contents

1. Motivation

It was in 1906 when Sir Joseph John Thomson mentioned in his Nobel prize speech ionized helium as propellant for space shuttles. He conceptually invented the electric propulsion.

After a long period where mostly chemical propulsion systems were used, the capacity of an alternative satellite propulsion system was recognized. Therefore, one also began to study electric propulsion systems. Their biggest advantage is a reduction of launching mass due to increased specific impulse compared with the widely used chemical thrusters. The higher impulse is gained by an increased propellant velocity. While the exhausted velocity of a chemical propellant is limited, charged particles can be accelerated infinitely by electric fields. The created ion beam produces the thrust of the satellite. With a higher specific impulse space missions can operate more flexible, while a reduced propellant mass reduces costs or lead to an increased payload.

For development and optimization of ion thrusters testing of a large number of expensive prototypes is necessary. These numbers can be reduced by an improved understanding of the physics of ion thrusters. This was the motivation of strong research activities in this field, in particular in numerical simulations of ion thrusters including their plumes.. The ultimate goal is to create a self-consistent model with predictive quality.

In this thesis, a kinetic Particle-in-Cell (PIC) code is used to study the physics of ion thrusters, especially the High Efficient Multistage Plasma Thruster (HEMP-T) patented by THALES. The work is split into two parts. In the numerical part a non-equidistant Poisson solver using the finite volume approach is developed and validated as a pre-requisite for non-equidistant PIC codes to allow a full resolution of thruster channel and plume. In the physical part results of PIC codes are used to analyze and characterize basic principles and characteristics of ion thrusters' plumes.

The outline of the thesis is as follows. In the first chapter the basics of plasma physics, ion thrusters and numerical methods will be explained. In chapter 3, state

of the art and new task of thruster simulations are given. The development and validation of a non-uniform Poisson Solver will be presented afterwards. As an example of an ion thruster, the basic physics of the HEMP-T, including the plume, is discussed using specific diagnostic modules for the PIC code. The newly developed Poisson solver allows a study of the effects of a domain extension on the results. Finally, the work is summarized.

2. Theoretical Basics

At the beginning of this chapter a short introduction into propulsion physics will be presented. It will introduce general aspects of plasma physics and the most important fundamentals of propulsion systems including an overview of existing concepts.

2.1. Basics of Propulsion System

The rocket equation which was published by Konstantin Tsiolkovsky in 1903 describes the change of velocity v for a rocket due to a propellant mass m_p and the exhaust velocity v_{ex} of the thruster. The derivation of this important equation [1] is given the following. One starts with the force T on the vehicle with the total mass M

$$T = M \frac{\mathrm{d}v}{\mathrm{d}t} \qquad (2.1.1)$$

where v is the velocity of the vehicle. The force is generated by the thrust of a propulsion system. The thrust is equal and opposite to the change of the momentum of the propellant in time. The momentum is given as the exhaust velocity of the propellant v_{ex} times the mass of the propellant m_p

$$T = -\frac{\mathrm{d}}{\mathrm{d}t}\left(m_p v_{ex}\right) = -v_{ex}\frac{\mathrm{d}m_p}{\mathrm{d}t} \qquad . \qquad (2.1.2)$$

The second equality is given since v_{ex} is constant in the spacecraft frame of reference. Since the propellant mass is decreasing, the total mass of the vehicle M is a function of the time

$$M(t) = m_p + m_d \qquad (2.1.3)$$

with m_d as the delivered mass. Since m_d is constant, one gets

$$\frac{\mathrm{d}M}{\mathrm{d}t} = \frac{\mathrm{d}m_p}{\mathrm{d}t} \qquad . \qquad (2.1.4)$$

2. Theoretical Basics

Using equation (2.1.2) and (2.1.4), equating with (2.1.1), one obtains

$$M\frac{\mathrm{d}v}{\mathrm{d}t} = -v_{ex}\frac{\mathrm{d}M}{\mathrm{d}t} \qquad . \tag{2.1.5}$$

Multiplying both sides by $\mathrm{d}t$ and dividing the equation by M gives

$$\mathrm{d}v = -v_{ex}\frac{\mathrm{d}M}{M} \qquad . \tag{2.1.6}$$

Integration from initial velocity of the spacecraft v_i to final velocity v_f, respectively from initial mass $m_d + m_p$ to final mass m_d yields

$$v_i - v_f = \Delta v = v_{ex} \ln \frac{m_d}{m_d + m_p} \qquad . \tag{2.1.7}$$

A characterizing value for thrusters is the specific impulse I_{sp}, which is given by the propellant exhaust velocity divided by the gravitational constant g. Therefore (2.1.7) can be rewritten as

$$\Delta v = (I_{sp}g) \ln \frac{m_d}{m_d + m_p} \qquad . \tag{2.1.8}$$

The distance which can be achieved during a mission is given by the thrust T integrated over the lifetime. For ion thrusters the exhaust velocity is nearly constant over the lifetime. The exhaust velocity of a chemical thruster is limited to approximately $3000\,\mathrm{m/s}$. The main goal of electric propulsion systems is to overcome this limit and therefore, to gain higher thrusts. One specific type of electric propulsion system is the ion thruster. Ion thrusters have a 5 to 10 times higher specific impulse than chemical thrusters and their mass is smaller [2]. Therefore, a reduction of launch mass by up to $1000\,\mathrm{kg}$ is reachable. Summarizing these advantages, a cost reduction or an increase of payload for commercial and scientific field missions deep into space seem to be possible. The idea of ion thrusters is to accelerate charged particles especially heavy noble gas ions using electric fields. Due to this basic plasma physics is needed to be able to understand the mechanism of ion thrusters.

2.2. Plasma Physics

All ion thrusters have in common that they operate with plasmas. A plasma is an ionized gas which consists of different species: electrons, neutrals and ions with different charges. A thermal equilibrated plasma exists, if the velocity distribution

function for each species is Maxwellian

$$f_s(\vec{v_s}) = \left(\frac{m_s}{2\pi k_B T_s}\right)^{3/2} \exp\left\{\frac{-m_s v_s^2}{2k_B T_s}\right\} \qquad . \tag{2.2.1}$$

Here k_B is the Boltzmann constant, T_s, m_s and v_s are the temperature, the mass and the velocity of each particle species s. With respect to the absolute value of the velocity $v = |\vec{v}|$ the velocity distribution function is given by

$$f_s(v_s) = 4\pi v_s^2 \left(\frac{m_s}{2\pi k_B T_s}\right)^{3/2} \exp\left\{\frac{-m_s v_s^2}{2k_B T_s}\right\} \qquad . \tag{2.2.2}$$

Therefore the average speed in an equilibrated plasma is

$$\langle v_s \rangle = \sqrt{\frac{8k_B T_s}{\pi m_s}} \tag{2.2.3}$$

and the root-mean-square velocity is given as

$$\sqrt{\langle v_s^2 \rangle} = \sqrt{3\frac{k_B T_s}{\pi m_s}} \qquad . \tag{2.2.4}$$

For each species the current j_s onto a plane is defined by

$$j_s = q_s \Gamma_s \tag{2.2.5}$$

with the flux density

$$\Gamma_s = \frac{1}{4} n_s \langle v_s \rangle \qquad , \tag{2.2.6}$$

where n_s is the density and q_s the charge of a species. In a plasma different charged species shield each other on length scales smaller than the Debye length.

$$\lambda_{D,s} = \sqrt{\frac{\epsilon_0 k_B T_s}{n_s q^2}} \qquad , \tag{2.2.7}$$

with the vacuum permittivity ϵ_0. The potential of a plasma includes a term from the normal Coulomb potential and an exponential term which describes the shielding due to different charges.

$$\phi(r) = \frac{q}{4\pi\epsilon_0 r} e^{-r/\lambda_D} \qquad . \tag{2.2.8}$$

This particular potential is named after two pioneers in plasma physics Peter Debye

and Erich Hückel, Debye-Hückel-potential. Therefore, charge separation exists only on length scales smaller than the Debye length. On larger length scales the plasma can be considered as "quasi neutral" therefore in this region the densities are given by

$$n_0 = n_e = Z \cdot n_i \qquad , \qquad (2.2.9)$$

with Z as the ion charge number. Charged particles react to electromagnetic forces. In plasmas, this can lead to charge separation, particle gyration and particle drifts. The Lorentz force of a particle s with charge q_s is given by the equation of motion

$$\dot{\vec{p}_s} = q_s(\vec{E} + \vec{v}_s \times \vec{B}) \qquad , \qquad (2.2.10)$$

with the electric and magnetic field $\vec{E}$ and $\vec{B}$. In a static magnetic field charged particles are accelerated parallel $\vec{E}$ with

$$\vec{a}_s = \frac{q_s}{m_s}\vec{E} \qquad , \qquad (2.2.11)$$

which leads to a charge separation due to the dependence on the sign of the particle charge. A static magnetic field leads to an oscillation of the particle in a plane perpendicular to the magnetic field with a frequency called cyclotron frequency ω_c and a radius named Larmor radius r_L

$$\omega_{c,s} = \frac{q_s B}{m_s} \qquad , \qquad r_{L,s} = \frac{v_{\perp,s}}{\omega_{c,s}} \qquad . \qquad (2.2.12)$$

In addition to this cyclotron movement, the particle moves along the field line with a velocity $v_{\parallel,s}$. $v_\perp$ and $v_\parallel$ are the perpendicular and the parallel component of the velocity with respect to the magnetic field $\vec{B}$. In ion thrusters electric and magnetic fields are used to accelerate heavy ions and generate a directed thrust.

In the present of electric and magnetic fields, particles have a drift velocity given by

$$\vec{v}_D = \frac{\vec{E} \times \vec{B}}{B^2} \qquad . \qquad (2.2.13)$$

Since the charge is not appearing in this equation no charge separation appears. This drift is named $\vec{E} \times \vec{B}$-drift or "Hall effect". Beside the cyclotron frequency there is another important time scale in a plasma. It is caused by a displacement of electrons with respect to ions. In case of such a displacement the Coulomb force

counteracts and pulls the electrons back. This happens with the so called plasma frequency of

$$w_{p,e} = \sqrt{\frac{n_e e^2}{\epsilon_0 m_e}} \qquad . \tag{2.2.14}$$

2.2.1. Plasma Sheath

Plasmas in thrusters are also strongly influenced by their wall contacts, therefore it is necessary to have a look at the plasma-wall physics. Close to a wall an equilibrated plasma with modified properties compared to the bulk plasma in the volume builds up, the plasma sheath. This sheath is characterized by a negative potential drop. In the bulk the plasma is quasi-neutral, whereas close to the wall one gets a charge separation, due to faster electrons reaching the wall. This potential drop has consequences for the velocity distributions and the particle densities.

A simple model for a plasma sheath assumes an ideal reflecting wall where recombination takes place only at the surface. A sketch of its characteristic is shown in Figure 2.1. In the bulk electron and ion densities are equal, whereas the average electron velocity is much higher than for the ions. Due to that, more electrons than ions impinge the wall and get absorbed there. Therefore, the electron density decreases near the wall and a negative potential drop develops. The potential difference between wall and bulk leads to accelerated ions in the sheath whereas electrons with energies smaller than $e\Delta\phi$ are reflected. Therefore, the electron density at the wall decreases stronger than the ion density like it is shown in Figure 2.1. This results in a steady state, where towards the wall ion flux and electron flux are equal.

$$\Gamma_e = \Gamma_i \qquad . \tag{2.2.15}$$

If one assumes zero net current at the wall ($j_e = j_i$) and quasi-neutrality ($Z n_i = n_e = n_0$), the potential drop between plasma and wall can be calculated according to [3] as

$$e\Delta\phi \approx -k_B T_e \ln\left(\sqrt{\frac{m_i}{2\pi m_e}}\right) \qquad . \tag{2.2.16}$$

The electron current density at the wall can be given as

$$j_e = -\frac{e}{4} n_e \langle v_e \rangle \exp\left\{\frac{-e\Delta\phi}{k_B T_e}\right\} \qquad . \tag{2.2.17}$$
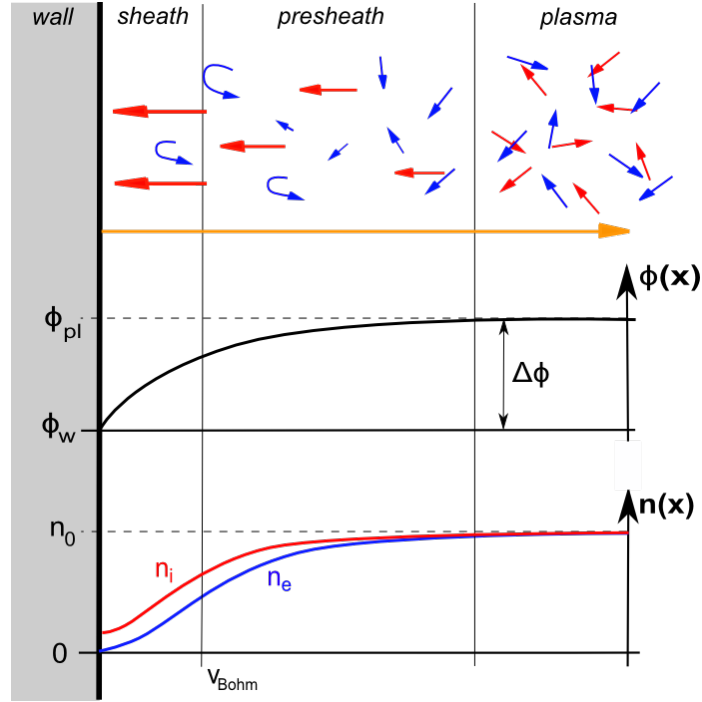
7

Figure 2.1.: sketch of processes in a plasma sheath; red arrows indicate the motion of ions, blue of electrons and orange of neutrals; potential at the middle and particle densities close to the sheath at the bottom

The ion density is decreasing towards the wall as well, but due to negative potential at the wall it does not get to zero. Close to the wall electrons neutralize impinging ions. As an assumption of this model the produced neutrals are reflected from the wall and again ionized in the bulk. In this simple model the sheath can be seen as collisionless. In reality processes like sputtering, secondary electron emission and radiation has to be taken into account. Between the sheath and the bulk plasma another region can be distinguished, the presheath. It is determined by the Bohm criterion. According to its discoverer David Bohm the following inequality is named Bohm-sheath criterion

$$v_{i,sh} \geq \sqrt{\frac{k_B T_e}{m_e}} = v_{Bohm} \qquad . \qquad (2.2.18)$$

This can be easily shown by using energy conservation and ion current density conservation. In addition the faster decay of electron density have to be taken into account to obtain the inequality. If one implements secondary electron emission at the wall, the potential drop is reduced. The additional electrons lead to an increased flux towards the wall in order to reach zero net current. Therefore, the modified effective potential according to [4] is given as

$$e\Delta\phi^{eff} = -k_B T_e \ln\left[(1-\gamma)\sqrt{\frac{m_i}{2\pi m_e}}\right] \qquad , \qquad (2.2.19)$$

where γ is the secondary electron emission coefficient. For this ansatz the electrons are assumed to have much higher temperatures than ions. Taking into account the secondary electrons, the most important effect is a reduction of the voltage drop near the wall. Therefore, one gets an increased number of electrons reaching the wall and as a consequence of the energy loss a lower electron temperature in the plasma bulk. For thrusters the sheath physics can become more complex as in the classical description. Two aspects have to be mentioned reasoning the disappearance of the classical Debye layer. At first electrons are essentially non-Maxwellian distributed and in addition the ceramics used for the inner walls of the thruster (BN, SiO_2, Al_2O_3) have secondary electron emission coefficients of $\gamma \approx 1$ for the electron energies hitting the wall. Therefore, the classical Debye sheath transforms into a double layer structure. Close to the the wall one gets a potential well, which leads to a trapping of a fraction of electrons. For higher electron energies the sheath begins to oscillate in time (GHz range) and in space (region larger than the Debye length). These oscillations are called sheath instability.

2.2.2. Interaction of Particles with Matter

After understanding how the wall influences plasma properties like potential or particle densities, the question of the following paragraph will be how plasma particles interact with the wall.

Particles impinging onto a surface are responsible for different effects. In addition to secondary electron emission, effects like sputtering, erosion and redeposition have to be understood. As explained in [5] the following processes are important to understand the dynamics of particles impinging onto a surface. The particles, neutrals, atoms or ions, are considered as projectiles that hit the surface. To penetrate the surface the projectiles must have energies in the range from eV to keV. An entering particle will be scattered at the atoms of the surface. These collisions lead to an elastic energy loss and a change in direction. Since the particle also interacts with electrons in the material an additional energy loss can be detected. Therefore, one must distinguish between two mechanism of loosing energy that slows down the projectile. The first is connected with heavy particle collisions. Positively charged ions are repelled due to coulomb force by the positive cores of the surface atoms. The

2. Theoretical Basics

Coulomb repulsion is screened by the electrons around the atoms. The second mechanism is an electric field drag created by the movement of the ion in a background of electrons. This slowing down can be seen as an analogon to viscous friction like a rock falling into water. Both processes are visualized in Figure 2.2.
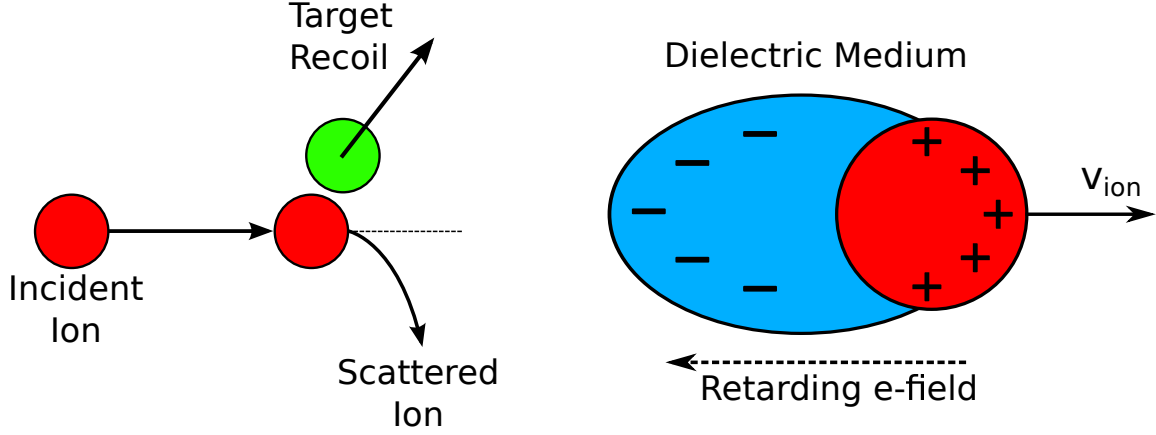

Figure 2.2.: left: nuclear collision, right: electronic stopping

The stopping power S can be written as the sum of these two processes. It is defined as energy loss per unit in length:

$$S = S_{nuclear} + S_{electronic} = \left(\frac{\mathrm{d}E}{\mathrm{d}x}\right)_{nuclear} + \left(\frac{\mathrm{d}E}{\mathrm{d}x}\right)_{electronic} \qquad . \qquad (2.2.20)$$

For lighter atoms with lower atomic numbers and for lower ion velocities respectively lower energies nuclear stopping is more important. Electron stopping is dominant for higher atomic numbers or higher energies. After loosing its whole energy the particle gets stuck in the surface. Another possibility is leaving the surface after some collisions as a backscattered projectile. But not only the impinging particle is of interest. During elastic collisions the kinetic energy of the projectile is transferred to recoil atoms. These again can be part of a similar process of collisions. The result is a collisional cascade. If the kinetic energy of a particle from the surface, gets large enough, it can get out of the surface. This is called sputtering. To get reasonable predictions for particle trajectories many particles and a large number of collisions have to be calculated. Therefore, simulations are useful tools to study particle-surface-interactions. Especially, for ion thrusters these processes have to be understood due to the influence of the channel surface on the plasma.

An often used code is SD.Trim.SP (Stationary/Dynamic Transport of Ions in Matter, with the calculation mode Serial and Parallel), which was developed by Andreas

Mutzke et al. [6] to study different effects resulting from interaction of particles with matter like sputtering, backscattering and transmissions effects of ion bombarded material. It makes use of the Binary Collision Approximation (BCA), which means that particle movement is treated as a series of inelastic binary collisions between atoms. For using the BCA assumption on the system are necessary, like an amorphous (randomized) material with a infinite lattice size and a temperature of $0\,\mathrm{K}$. This is acceptable for simulation of the plasma-wall contact, since the wall is always much colder compared to the particles of the plasma. The simulation domain of SD.Trim.SP is one dimensional with an x-coordinate perpendicular to the surface. In the static mode the following steps are proceeded: At the beginning, a projectile with kinetic energy E_0 and position $\vec{r}_0$ has to be initialized. After a distance λ one determines a collision partner with a statistically chosen impact parameter p. The impact parameter p is a function of the scattering cross section σ. Since SD.Trim.SP does not use a lattice, λ and p can be calculated directly by their distribution functions given as

$$f_1(\lambda)\,\mathrm{d}\lambda = \delta(\lambda - \lambda_0)\,\mathrm{d}\lambda \qquad , \qquad (2.2.21)$$

$$f_2(p) = \frac{\mathrm{d}\sigma}{\sigma} = 2\frac{p}{p_{max}^2}\,\mathrm{d}p \qquad . \qquad (2.2.22)$$

In (2.2.22) for the second equation σ is assumed as a circle with maximum impact factor p_{max}. Therefore, one can use $\sigma = \pi p_{max}^2$ and $\mathrm{d}\sigma = 2\pi p\,\mathrm{d}p$. The corresponding distribution functions are calculated by inverse Monte-Carlo sampling. Choosing a random azimuthal angle from $[0; 2\pi]$ between two collisions the BCA gives the resulting energies of the particles as well as both scattering angles θ_1 and θ_2 [5]. They determine the new direction of the projectile and the target atom. As the result of collisions with electrons the projectile atom loses energy. This loss is calculated as a continuous friction between two collisions.

Then for every particle there are three possible cases. If the energy of the particle is smaller than the binding energy of the material $E < E_b$ the particle gets stuck in the matter. If $E > E_b$ and the particle is close to the surface, the particle gets emitted as a sputtered atom. In both cases for this particle the simulation ends and it is not further followed. In the third case if $E > E_b$ an the particle is not close to the surface, it moves through the material and follows the steps described above, producing a collision cascade. A typical cascade is shown in Figure 2.3.
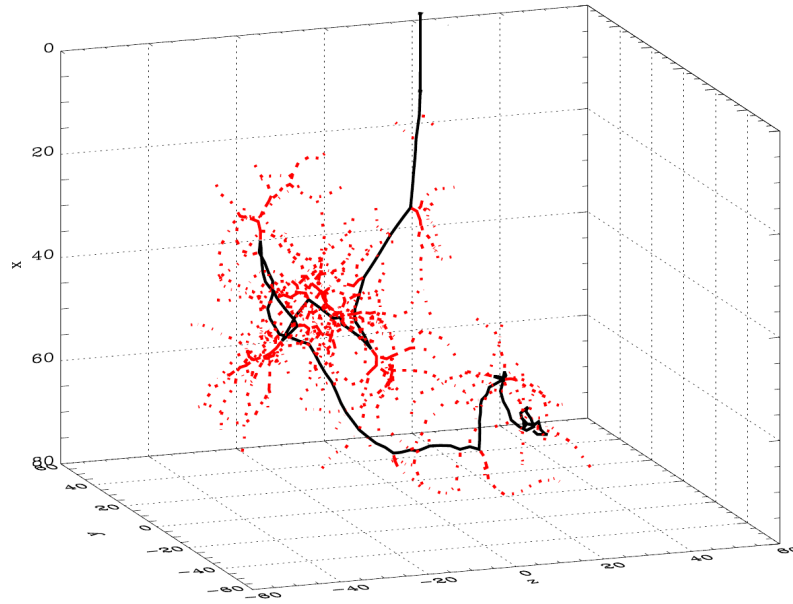
Figure 2.3.: simulated trajectory (black) and produced recoils (red) of a 2 keV He atom in Ni matter [6]

Depending on the number of particles, calculation and occupied memory for each collisional cascade becomes costly. With Tridyn, an other version of the code, also changes in surface composition can be included. Additional information about SD.Trim.SP can be found in [6].

2.3. Thruster Concepts

In the following different concepts for thrusters will be presented to give an overview of the development up to modern ion thrusters.

2.3.1. Grid Thruster

The first ion thrusters appeared in the early 1960's developed at the National Aeronautics and Space Administration NASA. This first type was a grid thruster. Its schematic structure is shown in Figure 2.4. It uses a radio frequency field to accelerate electrons to ionize the gas in a discharge chamber. As it can be seen in Figure 2.4 the chamber is terminated by two grids. The screen grid confines the plasma and is therefore positively biased. Whereas the acceleration grid is negatively biased to accelerate the produced ions.
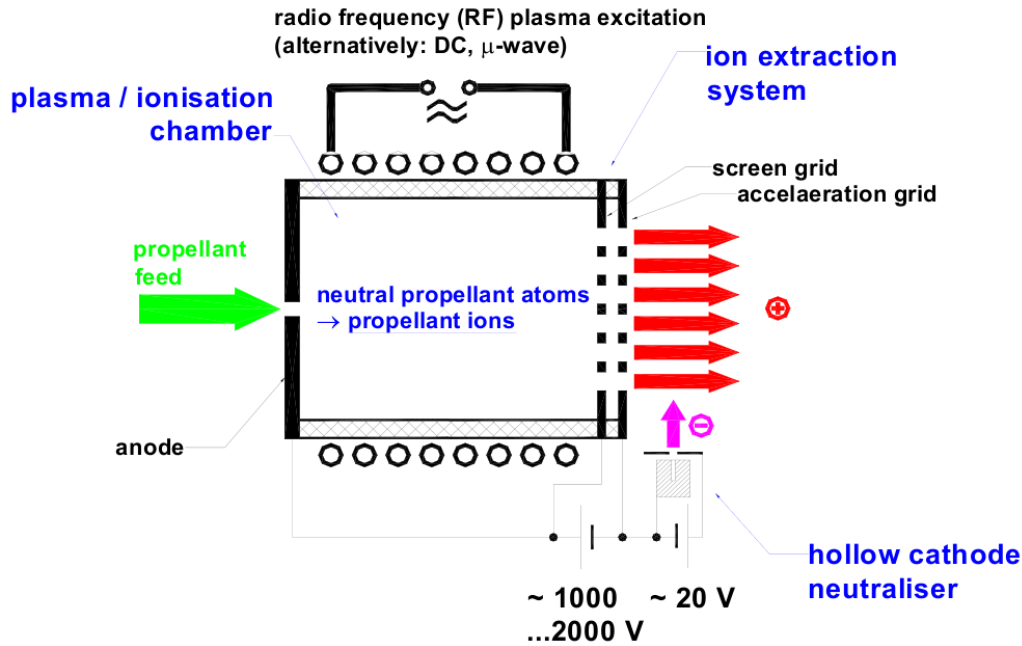
Figure 2.4.: scheme of an electric grid thruster

The field produced in the chamber accelerates electrons. Via collisions with neutral gas atoms the gas gets ionized. If ions come close to the grids and experience the plasma sheath at a grid hole, they will be accelerated by the potential drop between the two grids and produce the thrust by flowing out of the thruster. Ionization and acceleration are independent of each other, so they can be optimized separately. The main problem of such a grid thruster is the strong erosion of the grid produced by impinging ions. This erosion limits the lifetime and therefore makes it less attractive for economical applications. One way of overcoming this problem is the development of grid-free thrusters.

2.3.2. Stationary Plasma Thruster (SPT)

One type of grid-free thrusters are Hall Effect Thrusters (HET). A member of this family of thrusters is the Stationary Plasma Thruster. In current missions Hall Effect Thrusters are the most used ion thrusters, tested on many space missions like Astrium's geo-stationary Eurostar 3000 telecommunication satellite platform and ESA's Smart-1 mission [2]. The principle of Hall Effect thrusters is to ionize the propellant gas by trapped electrons using the Hall effect. To accelerate the produced ions an electric field is installed. In Figure 2.5 a schematic view of an SPT is shown.

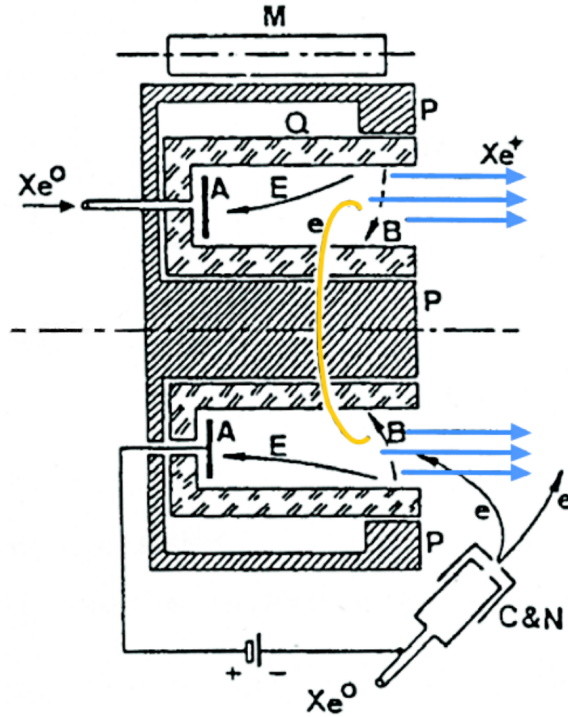The SPT consists of a ring shaped plasma channel with an inner radius $R_{in} \approx 30 \, \mathrm{mm}$

Figure 2.5.: scheme of a Stationary Plasma Thruster (SPT)

and an outer radius $R_{out} \approx 50\,\text{mm}$ and a channel depth of $L \approx 25\,\text{mm}$. A radial magnetic field towards the inner walls is produced by permanent magnets (P). A static electric field (E) is produced by an anode (A) and points outwards the thruster. It is perpendicular to the magnetic field. Since the electrons are magnetized, the Hall effect traps them in a circular movement in the plasma channel. These electrons are used to ionize the neutral Xenon gas. The generated positive ions are accelerated in the electric field, since they are only slightly affected by the magnetic field. They produce the thrust of the satellite.

Due to positive ions emitted by the thruster, the whole satellite gets negatively charged. This accelerates ions towards the satellite. The impinging ions produce damage, especially the solar panels can be strongly affected by sputtering. This reduces the lifetime of the satellite. Therefore, an electron gun is placed at the thruster exit. It neutralizes the Xenon ions to avoid damage of the satellite. In addition the neutralizer acts as a source for electrons, which get attracted by the anode and get trapped in the channel by the Hall effect. The electron energy determines the ionization rate and therefore the production of ions. It should be in the range of $15\ldots20\text{eV}$ for single charged Xenon ions. In this range the production of high energy ions is reduced and the damage of the satellite can be avoided. Therefore, high energetic

electrons have to be removed from the channel. In the SPT, this is done via secondary electron emission (SEE) at the thruster walls. Following the physics of a plasma sheath close to the wall ions and highly energetic electrons impinge the wall, whereas low energy electrons are reflected. The impinging electrons are absorbed, while the ions produce low energy secondary electrons. This leads to a cut-off in the electron energy distribution function at higher energies and the average electron temperature decreases. Due to the erosion at the channel wall the lifetime of SPT is limited, although it is about $1000\ldots2000$h longer compared to grid thrusters. Grid thrusters have a much steeper potential drop and therefore a much stronger acceleration of ions as the SPT.

2.3.3. High Efficient Multistage Plasma Thruster (HEMP-T)

1998 the THALES group patented the High Efficient Multistage Plasma Thruster (HEMP-T) [7]. It has the advantage of a strong potential drop as the grid thruster and a longer lifetime than the SPT thruster. Figure 2.6 shows the thruster channel of HEMP-T in a schematic view.
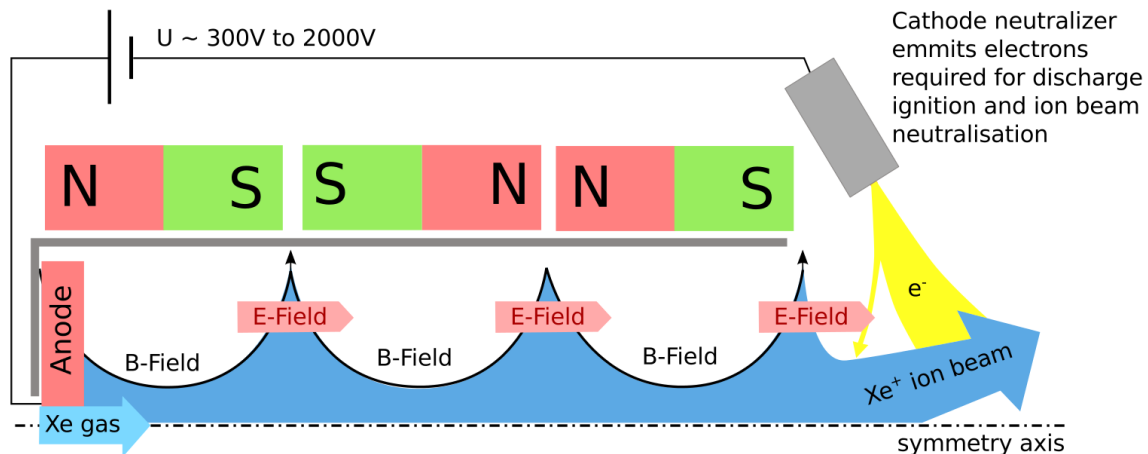

Figure 2.6.: schematic view of the High Efficient Multistage Plasma Thruster (HEMP-T)

It consists of an axial electric field due to the anode. An electron gun is placed at the thruster exit. In contrast to SPT the permanent magnets produce an axial magnetic field. The magnets face each other in a repulsive way. Only in a few regions, depending on the number of magnets, the magnetic field lines are perpendicular to the wall. These regions are called cusps. While in the SPT the whole channel is used to ionize the Xenon gas, in the HEMP thruster the ionization takes place more

pronounced in the cusps regions. Here, the Hall effect traps the electrons and forces them to a radial motion. Due to the strongly reduced wall contact, erosion on the thruster wall is reduced, which results in a much longer lifetime than the SPT. The lifetime is about $50\,00 \ldots 10\,000\,\mathrm{h}$.

For a further look into the physics of ion thrusters like HEMP-T or SPT simulations are used. Therefore, an introduction into numerical methods will be given in the following. In chapter 5 a characterization of HEMP-T is presented in more details.

2.4. Particle-In-Cell Method

In this chapter the numerical method used for simulations of ion thrusters will be introduced and explained. To understand the basic principles of a plasma the Particle-In-Cell (PIC) method is a powerful tool. In the first part the idea of this method will be introduced shortly.

PIC is a self-consistent method to simulate particles in velocity and position space. In addition one is able to include complicated atomic and surface interactions. Due to the very high number of particles ($\geq 10^{12}$) in a system it is not possible to use a direct particle model with full particle-particle interactions as in Molecular Dynamics. The well-known N^2 scaling of these interactions makes it impossible for simulations to resolve all Coulomb-interactions between all particles. Therefore, one solves the Poisson equations on a grid with N_g cells. Here N stands for the number of particles in a system. To compute the potential given by the Poisson equation only charge densities within each cell have to be known. So the PIC code calculates all macroscopic quantities at the grid points. Instead of solving the equations of motion

$$\dot{\vec{x}} = \vec{v} \tag{2.4.1}$$

$$\dot{\vec{v}} = \frac{q}{m}\left(\vec{E} + \vec{v} \times \vec{B}\right) \tag{2.4.2}$$

for each particle, one uses so called "super particles", which consist of thousands of real plasma particles. In (2.4.2) $\vec{x}$ denotes the position of a particle, $\vec{v}$ is its velocity, m its mass and q its charge. $\vec{E}$ and $\vec{B}$ are the electric and the magnetic field. The ansatz of super particles is possible, since all real particles within one super particle have the same charge/mass ratio and therefore follow the same trajectory as a solution of (2.4.2). PIC follows these trajectories, hence the methods gets its name

Particle-In-Cell method.

To get a correct simulation of the plasma, effects on the smallest length scale have to be taken into account, which is mostly the Debye length $\lambda_{D,e}$. This requests a grid with cell sizes of $\Delta x = 0.5\lambda_{D,e}$. The smallest time step of interest in a plasma is connected with the electron plasma frequency $\omega_{p,e}$. So the time step of the simulation is restricted by $\Delta t \leq \frac{2\pi}{\omega_{p,e}}$. Due to stability aspects while integrating the equations of motion $\Delta t = 0.2\frac{2\pi}{\omega_{p,e}}$ is used. In Figure 2.7 one cycle of the PIC algorithm is presented.
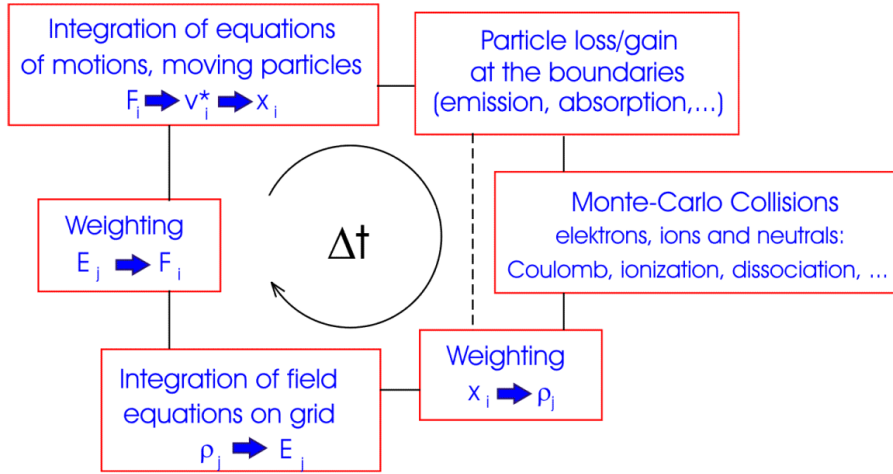

Figure 2.7.: Particle-In-Cell method: one cycle

To start, charge densities ρ are interpolated from the particle position $\vec{x}$ to the grid points X_i with $i = 1, \ldots, N_g$ using a weighting function. Then the Poisson equation

$$\Delta\phi_i = -\frac{\rho_i}{\epsilon} \tag{2.4.3}$$

is used to calculate the electric potential ϕ_i on each grid point i, out of this the electric field is calculated at the grid. Afterwards, the same weighting function as before is used to interpolate the electric field back to the particle positions $\vec{x}$. If another weighting scheme is used self forces might be created. Now the equations of motion can be solved for each particle at its exact position. This subroutine is called particle mover or pusher. Afterwards the algorithm allows to calculate particle loss and gain at the boundaries and in the next step different types of collisions concerning all particle species are implemented in a Monte Carlo Collision method. The next time step follows and again the particles were interpolated to the grid. So the PIC cycle is repeated The PIC code delivers a complete microscopic description of the

plasma with the possibility to diagnose all quantities like potential, particle densities, velocities and temperatures. several times. Further details about PIC are given in [8].

In this thesis a 2 dimensional axially symmetric PIC code with 3 dimensions in velocity space is used. The code only uses non-dimensional variables. Lengths are scaled to the Debye length as the smallest length scale. Times are scaled by the inverse electron plasma frequency as the smallest time scale of interest. This way one gets the following scaling:

$$\tilde{\Delta} t = \omega_{p,e} \Delta t = 0.2 \tag{2.4.4}$$

$$\tilde{\Delta} z = \frac{\Delta z}{\lambda_{D,b}} = 0.5 \tag{2.4.5}$$

Consequently, the velocities scale by:

$$\tilde{\Delta v_s} = v_s \frac{\Delta t_s}{\Delta z} = v_s \frac{0,5 \tilde{\Delta t_s} \lambda_{D,b}}{\omega_{p,e}} \tag{2.4.6}$$

The subscripted s stands for each particle species. Ions and neutrals are often not calculated in every timestep. The so called subcycling allows to update these particles after n steps of electrons. The code used for this work has a subcycling factor of 400 for ions and 2000 for neutrals. Additionally, one applies a self-similarity scaling to reduce numerical costs. The length and all connected quantities like potential, magnetic field, mass flow rate and temperature can be scaled by a scaling factor. This reduces the computational costs, but keeps the relevant non-dimensional parameters of the system constant. These constant parameters are the Knudsen number for ionization and the Hall parameters for the confinement. The Knudsen number is defined as the ratio of the molecular mean free path length divided by a representative physical length scale of the system. The Hall parameter is the ratio between the electron gyrofrequency and the electron-heavy particle collision frequency. In the current code a self-similarity scaling factor of $\zeta = 0.1$ was implemented. Therefore the size of the system is 10 times larger in reality than in the simulation.

2.4.1. The Poisson Solver

This thesis puts particular emphasis on one element of the PIC cycle, the calculation of the potential using the Poisson equation (2.4.3). This element is often called solver. There are different methods available to do this task, for example the finite volume

method. In the following this method will be described in detail.

The finite volume method (FVM) describes an algorithm which allows to evaluate the solution of partial differential equations. It is therefore well suited for the problem of solving the Poisson equation. In many other PIC codes the finite difference method is used, but as it will be presented in this work, there are several advantages to use the FVM. The idea behind the FVM is to calculate fluxes instead of derivatives as in the finite difference method. This is done by applying Gauss' law.

In the following the FVM will be described by following some trivial analytic examples regarding to the derivation of numerical heat transfer of Patankar [9]. The conservation of flux for a one dimensional grid is

$$\frac{d}{dx}\left(k\frac{dT}{dx}\right) + S = 0 \qquad , \tag{2.4.7}$$

with S as a source and k as a transport coefficient for the temperature T. The temperature can be identified by any other physical entity which is transported via diffusion. This describes the flux through the grid shown in Figure 2.8
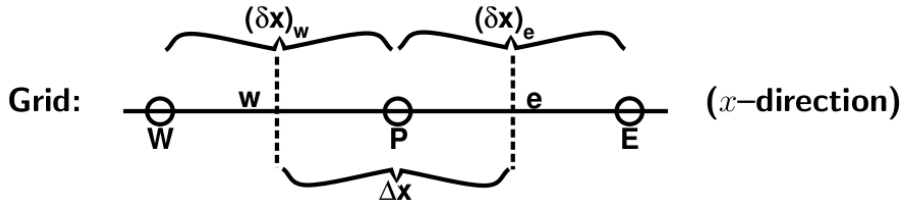

Figure 2.8.: scheme of a uniform 1-dimensional grid

where the faces of the control volume are represented by dashed lines. Integrating over the control volume leads to

$$\left(k\frac{dT}{dx}\right)_e - \left(k\frac{dT}{dx}\right)_w + \int_w^e Sdx = 0 \qquad . \tag{2.4.8}$$

To solve this equation the values for $\frac{dT}{dx}$ are needed at the boundaries. Therefore, one has to make an assumption about a profile in one cell. The simplest choice is to take a constant profile of T in the cell. In this case the derivatives at the boundaries would not be defined. Therefore one has to take at least a piecewise-linear profile achieved by interpolation between two neighboring points. By assuming this profile the discrete equation is given as

$$\frac{k_e\left(T_E - T_P\right)}{(dx)_e} - \frac{k_w\left(T_P - T_W\right)}{(dx)_w} + \bar{S}\Delta x = 0 \qquad , \tag{2.4.9}$$

2. Theoretical Basics

where $\bar{S}$ is the averaged value of S over the control volume. Rearranging the terms and introducing new coefficients one gets:

$$a_P T_P = a_E T_E + a_W T_W + b = \sum_{all\ neighbors} a_{nb} T_{nb} + b \qquad (2.4.10)$$

with $a_E = \frac{k_e}{(dx)_e}, a_W = \frac{k_w}{(dx)_w}$, $a_P = a_E + a_W$ and $b = \bar{S}\Delta x$.

In radial geometries the creation of a singularity at the axis due to the discrete calculation scheme is a large problem of the finite difference method. This singularity is not appearing in the FVM, since a boundary condition of zero flux at the axis can be directly applied. In similar ways other boundary conditions can be implemented very simple, including the implementation of dielectrics.

Especially for this work an other advantage of FVM is very important. For non-equidistant grids, which will be described later as one of the goals of this work, a finite volume method is much easier to implement. This results from the fact that gradients, perpendicular components and boundary integrals are directly given by geometrical information of the grid.
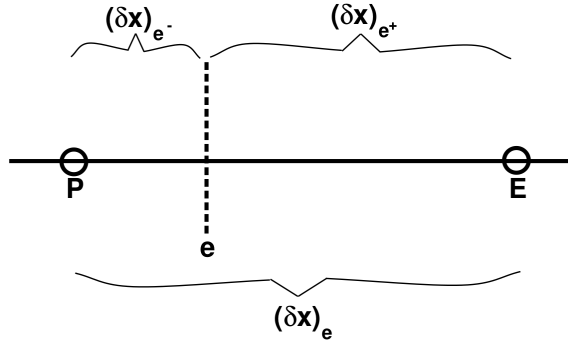

Figure 2.9.: scheme of a nonuniform 1-dimensional grid

There is only one aspect one must take into account, when using a grid as in Figure 2.9. The transport coefficient of the general equation can not be calculated using the arithmetic mean. One can show that the arithmetic mean gives wrong results within some limits, for example if $k_E \to 0$ or $k_P \gg k_E$. Following Patankar [9] one has to use the harmonic average, which is given in one dimension by:

$$k_e = \left(\frac{1 - f_e}{k_P} + \frac{f_e}{k_E} \right)^{-1} \qquad (2.4.11)$$

with $f_e = \frac{(dx)_{e+}}{(dx)_e}$.

20

The Poisson equation used for PIC can be seen as a pure diffusion equation like. One can identify ϵ as the transport coefficient and the potential ϕ analogous to the temperature T. Therefore, the discretization for the one dimensional Poisson equation using the FVM is given by:

$$\frac{\epsilon_e \left(\phi_E - \phi_P\right)}{(dx)_e} - \frac{\epsilon_w \left(\phi_P - \phi_W\right)}{(dx)_w} + \bar{\rho}\Delta x = 0 \qquad . \qquad (2.4.12)$$

In chapter 3 an additional motivation and physical explanation why the coarsening of the grid is necessary to do further studies of ion thruster physics is given.

3. State of the Art and New Tasks

In the past many physicists used the Particle-In-Cell method to analyze the behavior and the characteristics of ion thrusters. After numerous works using fluid or hybrid codes with the assumption of a Maxwellian distribution for electrons and kinetic ions, with the improvement of computing resources over the past decade self-consistent PIC codes are developed to study ion thrusters in full detail. In 2009 Konstantin Matyash published his work about HEMP and SPT thrusters [10]. Figure 3.1 shows his results of a self-consistent PIC simulation for the HEMP DM3a thruster. He implemented 890×240 grid points to simulate a radial length of $24\,\text{mm}$ and an axial length of $89\,\text{mm}$. At $z = 0$ an anode with $500\,\text{V}$ was used.
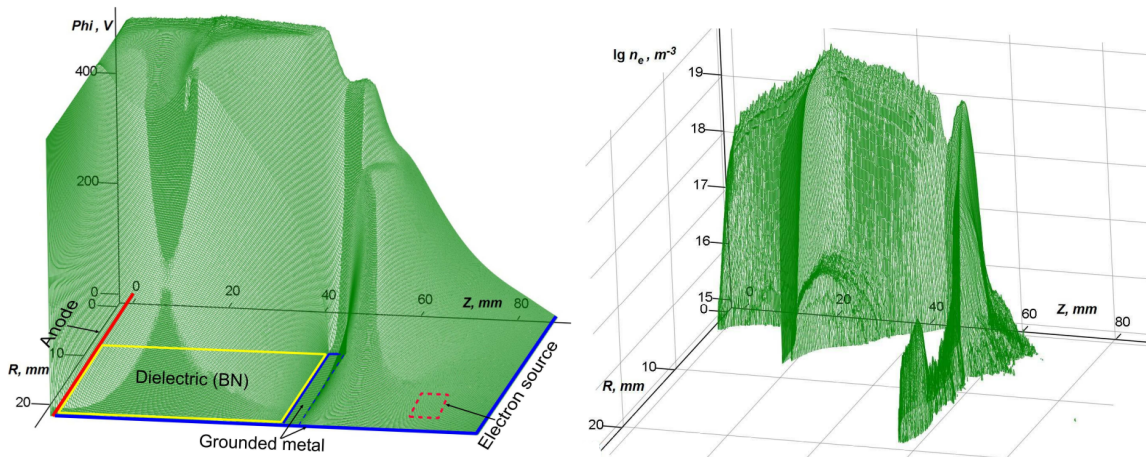

Figure 3.1.: potential (left) and electron density on a logarithmic scale (right) of a HEMP thruster including near-field plume [10]

In the potential plot one can see that in the whole channel the potential is nearly constant. It has a strong drop at the thruster exit, which leads to high accelerations of ions in this region. This potential profile is similar to one of a grid thruster. It is known as one of the advantages of HEMP-T. At the plot right hand side one can see that the electron density is concentrated at the inner part of the channel. The contact to the channel walls is limited to the cusp region at $z \approx 19\,\text{mm}$. Therefore HEMP-T

has the advantage of very small erosion in the channel and is often summarized with the slogan of a "grid-free grid thruster with minimized erosion".

To be able to address the problem of interaction of ion thrusters' plume with the satellite some short-comings of the existing simulations have to be overcome. The most prominent disagreement of simulations and experiments in the past was the large difference in the angular distribution of ions, which can be seen in Figure 3.2
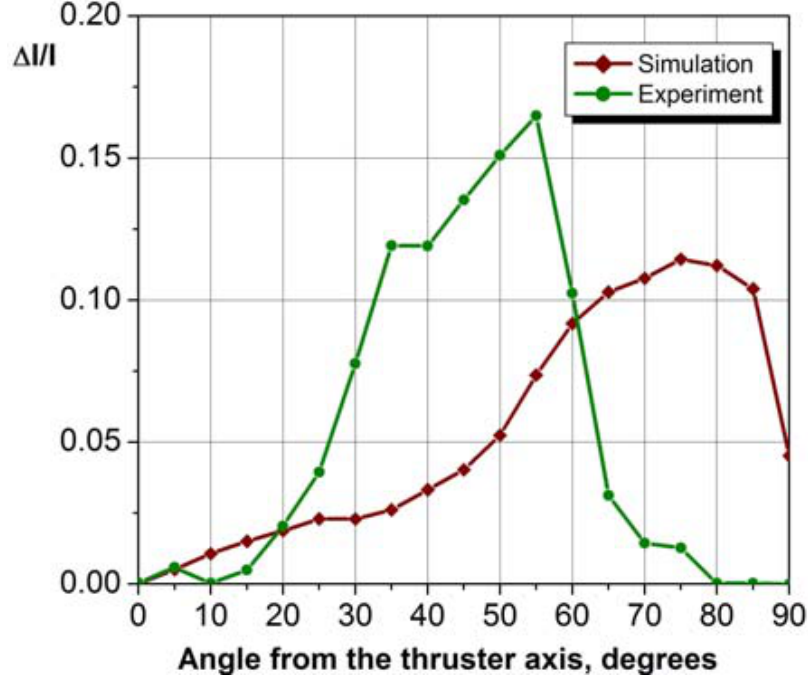

Figure 3.2.: angular distribution of ion current contribution scaled to total ion current [11]

The most promising ansatz to improve the simulation quality in the plume region is to extend the size of the domain. In smaller domains the boundary conditions have a strong impact on the potential, which can cause numerical artifacts in [11]. However, a larger domain size leads automatically to much longer computational times. As it was explained in chapter 2, PIC codes require cell sizes that resolve the Debye scale. Since for PIC the solver is the most costly part, a coarser grid can significantly reduce computational time. For plume simulations a non-equidistant grid is possible, because the Debye scales of the channel and the plume are quite different. According to equation (2.2.7) the Debye length can be estimated for the electrons in the thruster channel by $\lambda_{D,e} \approx 14.8\,\mu m$, whereas in the far-plume region it is about $\lambda_{D,e} \approx 1.3\,mm$. The Debye length of the ions is even larger. Therefore, one can use much larger cells in the plume and try to extend the domain to a size,

where one gets independent of the boundary conditions.

If one is able to extend the size of the domain, one can study the plume physics in detail, which is up to now one of the most important open questions in thruster physics. To extend the PIC code into a non-equidistant PIC code one has to make changes in each part of the PIC cycle. In this thesis the main focus is on the Poisson solver. The finite volume method will be used to develop a non-equidistant Poisson solver. Additional adaptions, not discussed here, are needed also in the pusher part to avoid the appearance of artificial self-forces producing errors in the momentum balance.

4. Development and Testing of a Poisson Solver

4.1. Numerical Development of the Algorithm

One of the goals of this work is to implement a nonuniform two-dimensional grid for the solution of the Poisson equation using the finite volume method (FVM). The Poisson equation is given by

$$\Delta\phi = -\frac{\rho}{\epsilon} \qquad .\tag{4.1.1}$$

It is pure diffusion equation analogous to the heat flux transport. The electric field can be calculated as the flux. Let us start with the simple example of a uniform two dimensional grid like in Figure 4.1:
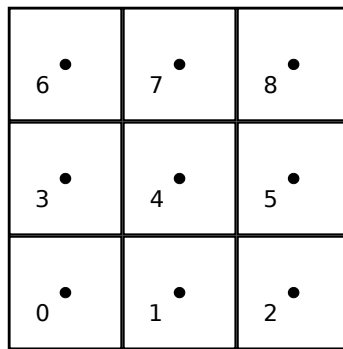

Figure 4.1.: uniform two dimensional grid

The idea of the FVM is to loop over each cell and to calculate the flux between the cell and its neighbors. The matrix entry $A_{i,j}$ describes the coefficient for the flux between cell i and cell j and is calculated as:

$$A_{i,j} = \epsilon_{i,j}\frac{dA_{i,j}}{dx_i} \qquad .\tag{4.1.2}$$

4. Development and Testing of a Poisson Solver

With the assumption that all cells have the same properties with grid sizes $dx = dy = 1$, surface boundaries $dA = 1$, volumes $dV = 1$ and permittivity $\epsilon_r = 1$ one gets the following system of equations written in matrix notation:

$$
\underbrace{\begin{pmatrix}
-2 & 1 & & 1 & & & & & \\
1 & -3 & 1 & & 1 & & & & \\
& 1 & -2 & & & 1 & & & \\
1 & & & -3 & 1 & & 1 & & \\
& 1 & & 1 & -4 & 1 & & 1 & \\
& & 1 & & 1 & -3 & & & 1 \\
& & & 1 & & & -2 & 1 & \\
& & & & 1 & & 1 & -3 & 1 \\
& & & & & 1 & & 1 & -2
\end{pmatrix}}_{A}
\begin{pmatrix}
\phi_0 \\ \phi_1 \\ \phi_2 \\ \phi_3 \\ \phi_4 \\ \phi_5 \\ \phi_6 \\ \phi_7 \\ \phi_8
\end{pmatrix}
=
\begin{pmatrix}
\frac{\rho_0}{\epsilon_0} \\ \frac{\rho_1}{\epsilon_0} \\ \frac{\rho_2}{\epsilon_0} \\ \frac{\rho_3}{\epsilon_0} \\ \frac{\rho_4}{\epsilon_0} \\ \frac{\rho_5}{\epsilon_0} \\ \frac{\rho_6}{\epsilon_0} \\ \frac{\rho_7}{\epsilon_0} \\ \frac{\rho_8}{\epsilon_0}
\end{pmatrix}
\qquad (4.1.3)
$$

The next step is to implement a coarsening in the grid. The algorithm itself will be still the same, only some geometrical information are changed. Therefore, the scheme of a non-equidistant grid shown in Figure 4.2 is used.

Figure 4.2.: non-equidistant 2 dimensional grid

The small cells in the left lower corner are the same as in the equidistant case with $dx = 1$, $dA = 1$ and $dV = 1$. Cell $8 \ldots 12$ are doubled in length and so $dx = 2, dA = 2$ and $dV = 4$. If one follows the same algorithm as in the equidistant case, one will get the following discretization matrix.

$$
A = \begin{pmatrix}
-2 & 1 & 1 & & & & & & & & & & & & \\
1 & -2\frac{2}{3} & & 1 & & & & & & \frac{2}{3} & & & & & \\
1 & & -3 & 1 & 1 & & & & & & & & & & \\
& 1 & 1 & -3\frac{2}{3} & & 1 & & & & \frac{1}{2} & & \frac{1}{6} & & & \\
& & 1 & & -3 & 1 & 1 & & & & & & & & \\
& & & 1 & 1 & -3\frac{2}{3} & & 1 & & \frac{1}{6} & & \frac{1}{2} & & & \\
& & & & 1 & & -2\frac{2}{3} & 1 & \frac{2}{3} & & & & & & \\
& & & & & 1 & 1 & -3\frac{1}{3} & \frac{1}{2} & & & \frac{1}{2} & & \frac{1}{3} & \\
& & & & & & \frac{2}{3} & \frac{2}{3} & -2\frac{1}{6} & & & & & \frac{5}{6} & \\
& \frac{2}{3} & & & \frac{2}{3} & & & & & -3\frac{1}{6} & 1 & \frac{5}{6} & & & \\
& & & & & & & & & 1 & -2 & & 1 & & \\
& & \frac{2}{3} & & & \frac{2}{3} & & & & \frac{5}{6} & & -4 & 1 & \frac{5}{6} & \\
& & & & & & & & & 1 & 1 & -3 & & & 1 \\
& & & & & & & 1 & & & & 1 & & -3 & 1 \\
& & & & & & & & & & & & 1 & 1 & -2
\end{pmatrix}
$$

$$(4.1.4)$$

In both cases at the boundaries zero flux is used. Another possibility is to set the boundary cells to a fixed potential value, this is even simpler. In this case one only has to set the value at the main diagonal to 1 and all other matrix values for this cell to 0. With the algorithm described here, one is able to discretize non-equidistant grids. The only missing part to solve the system of equations is the right-hand side, but this is trivially the vector of charge densities in every cell.

The solution of the matrix equation is done by decomposing the matrix into a lower triangular matrix and an upper triangular matrix. This needs to be done only once in the PIC code, after initializing the grid with its geometrical information. During the PIC cycle only the very fast backsolve with the updated right hand side has to be done at every time step. The LU decomposition and the backsolve use the SuperLU package [12].

In the following different benchmark tests will be done. The goal is to find the best method to solve the Poisson equation in the PIC code, which will be used to study the plume of ion thrusters.

4.2. Numerical Tests

In the first part of the following section two methods of treating the simulation domain for the solver including non-equidistant meshes will be discussed. The major work is to derive the discretization matrix of the Poisson equation as shown in chapter 2. The inversion of this matrix and the solution of the Poisson equation for the potential is done using the SuperLU package [12].

There are different ways of combining domains and treating them in the matrix as one will see. The first idea is to put the complete discretization of the whole system into one big matrix and solve it. This has the advantage that all interpolations are done in the step of calculating the matrix elements, but the matrix to be inverted gets rather large. Another concept is to create two different domains nested into each other. One uses the large domain over the whole simulation area with a coarse grid. This mesh is solved and defines then boundary conditions for a finer mesh in sub-parts of the domain.
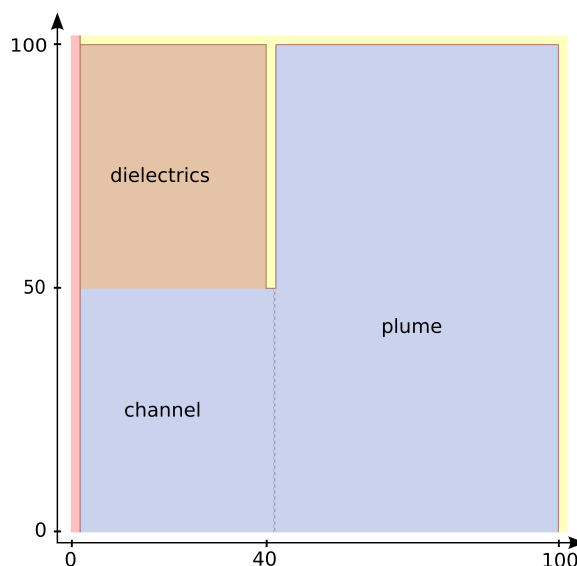
Figure 4.3.: test domain for analyzing different methods

To be able to compare the different approaches one creates a test case presented in Figure 4.3. This test mesh is smaller than the mesh that will be used for the PIC code later. The reduced size is necessary to be able to solve on the fine mesh as a reference solution for the complete domain within acceptable limits of memory and computing time. The test domain consists of a 102 times 102 grid cells. The left border, drawn with yellow, indicates an anode that is set to the fixed value of 4. Due

to the scaling of variables in the PIC code as mentioned in chapter 2 this represents $400\,\mathrm{V}$. For $0 < z < 40$ and $50 < r < 100$ (upper left corner of Figure 4.3) there is a dielectrics with ($\epsilon = 4$). At the axis (at $r = 0$) a zero flux boundary condition is used. The outer boundary at $z = 60$ is set to $\phi = 0$. For the outer boundary at $r = 100$ and $z = 100$ one can decide between zero potential or zero flux (zero electric field) boundary conditions. A typical solution is shown in Figure 4.4.
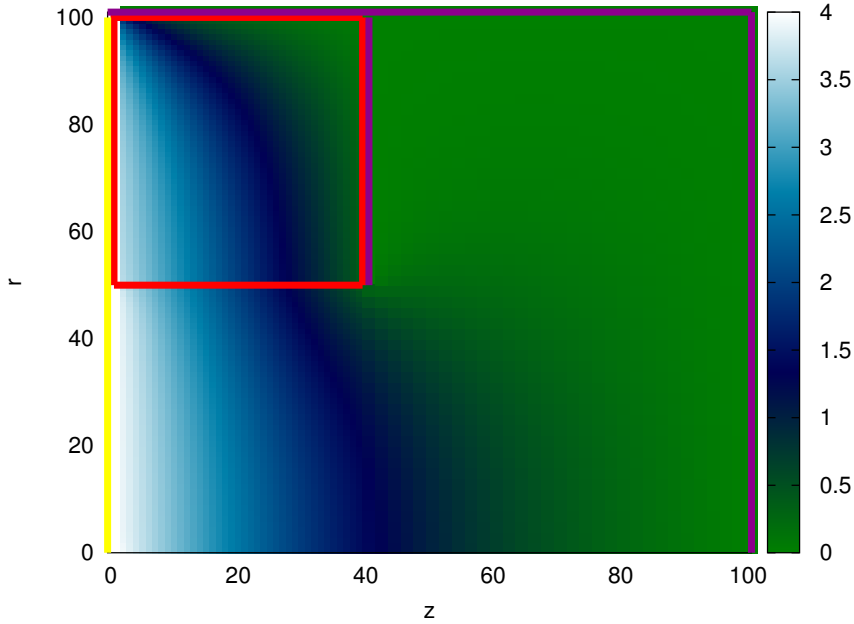
Figure 4.4.: potential ϕ color encoded for the test domain with a fine grid of 1×1 cells including an anode (yellow), a dielectrics (red) and $\phi = 0$ boundary conditions (violet)

In the following this test system will be solved with different approaches to study their advantages and disadvantages. A further description and a comparison of these methods will be given.

4.2.1. One-Grid Approach

The first idea is to treat the whole simulation domain within one matrix using the finite volume method. The disadvantage of this idea is that one creates matrices of $N_G \times N_G$ size. This gives very huge matrices with rather long computing times to solve. One applies the rules of the finite volume method that were already discussed in the basics part of this thesis in chapter 2.

The first test case will include only one jump in cell sizes from 1×1 cells to 2×2

cells. Within the dielectrics and the channel cells with size 1×1 are used, in the plume the 2×2 cells have twice the size of the ones in the channel. The matrix is filled up according to the finite volume method. After filling up the matrix and solving the system of equations, one gets the solution for the potential in vacuum. In the first calculation the borders at $r = 100$ and at $z = 100$ are set to a fixed value of 0. Changing these boundary conditions to zero flux (zero electric field), one gets a similar result. To get a better understanding of differences of both solutions, Figure 4.5 shows profiles from the potential at two different positions $r = 11$ and $r = 65$.
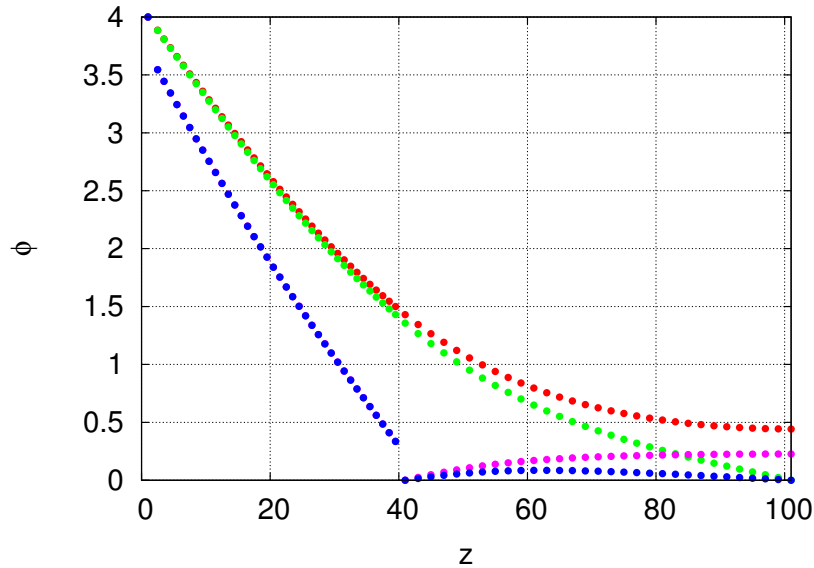
Figure 4.5.: cuts at different positions with different boundary conditions: r=11 with no flux boundary condition (b.c.) in red, r=11 with fixed value b.c. in green, r=65 with no flux b.c. in violet, r=65 with fixed value b.c. in blue

As one would expect the solutions with zero flux at the boundary has larger values in the plume than the solution with fixed values at the borders. This results from the strong impact of the boundaries in such a small domain. Later in the PIC simulation the domain has to be so large that there will be at most negligible differences in the outer part of the plume. One can compare the result of the run with a coarsening with the fine grid solution. Plotting the difference between the run with coarsening and the run with the fine grid for the whole domain one can diagnose the differences. This is done in Figure 4.6.

The largest differences occur in the region of the coarsening jump at $z = 40$. Afterwards with increasing z the difference decreases again. In the channel the difference
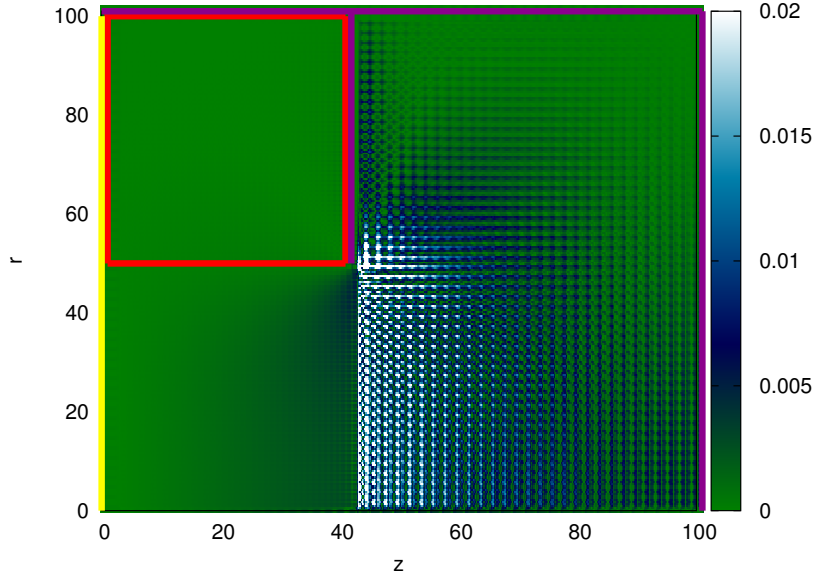
Figure 4.6.: absolute difference $\Delta\phi$ between the fine solution and the solution with one coarsening level

is very small. The coarsening has obviously no large impact on the fine grid.

Runtime Analysis for the One-Grid Approach

The goal of this chapter will be to study the runtime of this algorithm and to find a limit, how large the domain can become. Different sizes of grids are used to test how long this algorithm needs to calculate the vacuum potential. Each time the matrix is filled, decomposed and one backsolve is done. One has to take into account that all these things, except the backsolve, are done only once before the PIC cycle. The backsolve is repeated every timestep, so its time is extraordinarily important. For the backsolve the practical limit is to stay below 1 s.

To study the real physical behavior of an ion thruster it is necessary to enlarge the simulation domain of the runs, that have been performed up to now [10]. To find out how large the domain with the presented algorithm can be before one reaches the runtime limit, the following tests are done. The grid shown in Figure 4.7 is implemented to have a flexible domain size and be able to measure the runtime.

The domain includes the thruster as already used in the first test grid with an anode at z=0 (red), a dielectrics (brown) and the channel (dark blue). The above border colored in red is coded as fixed potential $\phi = 0$ to act as metal boundary. This whole region and the near-field (darkest part outside the thruster) are implemented with cells of size 1×1. Then up to $r = 1000$ and $z = 1000$ cells with size 2×2 are
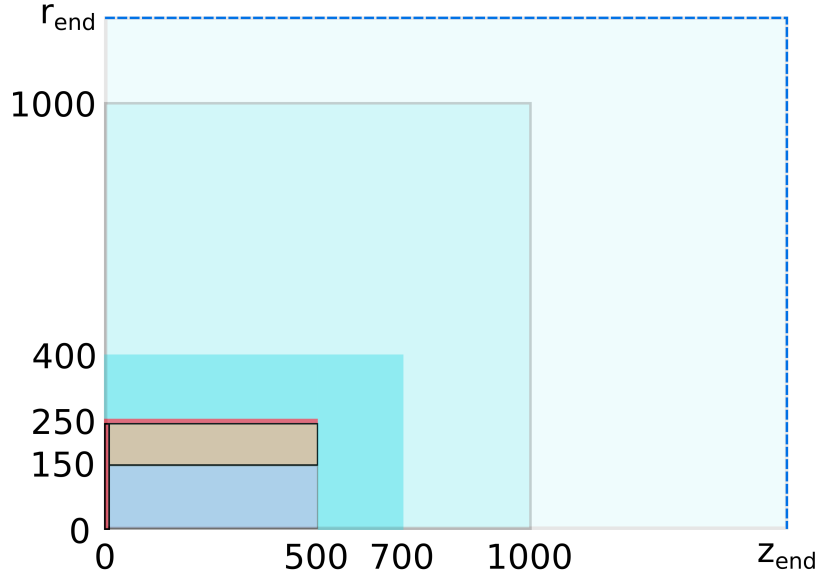
Figure 4.7.: domain to test different positions of splitting

used. The outer part of the plume (lightest region) consists of 4×4 cells and ended at variable distances r_{end} and z_{end}. In dependency to r_{end} and z_{end} the number of cells in the grid N_G will change. The thruster, the near field and the first part up to $r = 1000$ and $z = 1000$ consists already of 460000 cells and is larger than older runs [10].

Important variables to quantify the discretization matrix of the grid are the number of non-zero elements $nnz(A)$ and the sparsity of this matrix $sparse(A)$. The sparsity is defined as the ratio of non-zeros elements to the total number of elements. Both are shown in Figure 4.8 for different grid sizes.
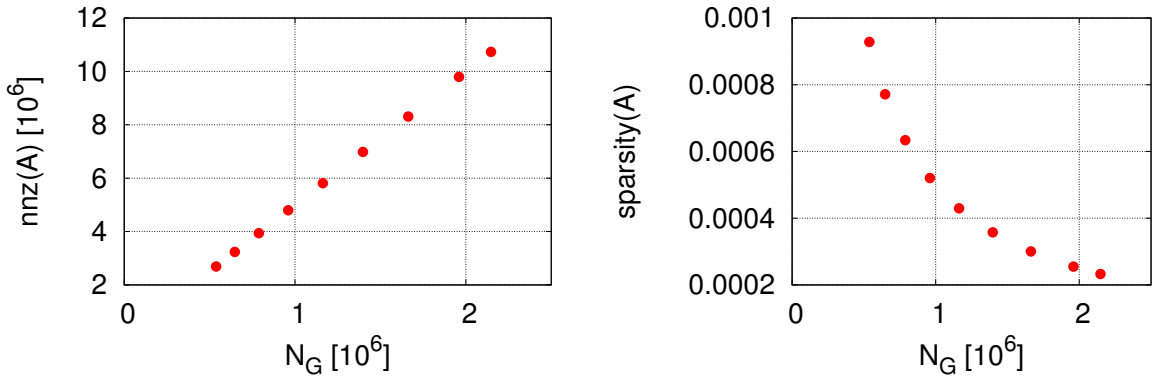
Figure 4.8.: number of non-zero elements (left) and sparsity (right) of the matrix A for different number of grid points N_G

The left part shows the linear scaling of the non-zeros over N_G. The right shows

that with increased N_G the sparsity of matrix decreases. The sparsity is calculated as follows:

$$sparse(A) = \frac{nnz(A)}{N_G^2} \propto \frac{1}{N_G} \qquad . \qquad (4.2.1)$$

As shown the number of non-zero elements scales linear with the number of grid cells. Therefore, the sparsity scales with $\frac{1}{N_G}$, which is consistent with the right part of Figure 4.8. After decomposing the matrix A into L and U one can make similar analysis for both. One detects the same scaling for both matrices like for A, only the values for $nnz()$ and $sparse()$ are a bit higher. Even these matrices are quite sparse, which makes the backsolve fast.

The times for initialization of the grid and the filling of the matrix scale quadratic with the number of grid cells. As explained before, more important for the PIC application is the backsolve time. The result of its measurements is shown in Figure 4.9.
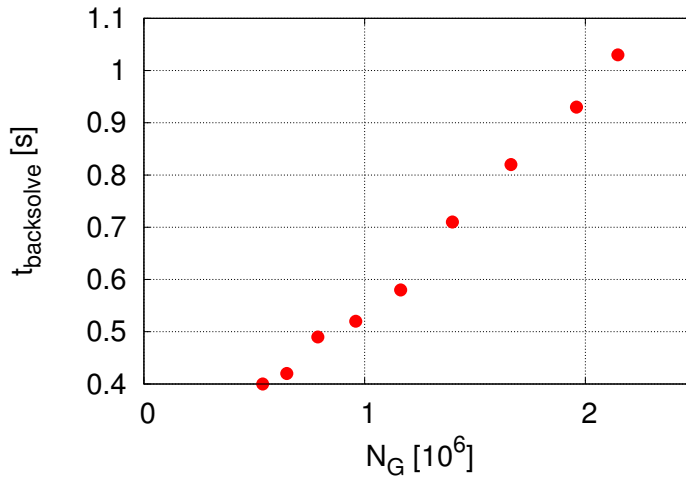
Figure 4.9.: backsolve time as a function of number of grid points N_G

For the PIC cycle from experience one needs a backsolve time below one second. It seems to be uncritical for this two-dimensional code to reach grid sizes near 2×10^6 cells. The main part of the work for the code is the initialization of the grid, including the search for neighbors and the filling of the matrix. This process can take quite long, but since it will be performed only once in PIC this is no problem. An extension of the PIC code to a third dimension the solver defines a critical runtime limit. Therefore, one has to search for alternatives.

4.2.2. Hierarchical Multi-Grid Approach

A second method treating non-equidistant meshes will be presented in the following. With this ansatz it is not necessary to use one huge matrix. So it will be possible to save computation time and memory. In addition a decomposition of the domain and parallelization of the code become easier possible.

At first a coarse grid on the whole domain is used. The values from that solution are used as boundary conditions for the finer mesh, where only subdomains of the domain are solved. Afterwards the fine solution is interpolated back to the coarse grid. This procedure can be redone arbitrarily often. So a specific solution can be iterated. For a first test a grid with cell size 2×2 were implemented over the whole domain as the coarse mesh. The channel $r < 50$ and $z < 40$ is the region of the finer grid with 1×1 cells.
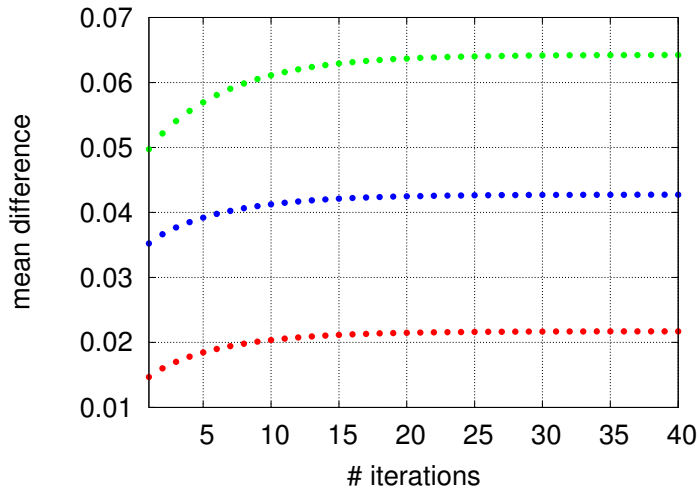
Figure 4.10.: mean difference $\Delta\phi$ after each iteration: plume (red), channel (green), whole domain (blue)

It is possible to iterate a specific solution with this method, so at first the iterative character has to be studied. Therefore, one compares the solution after each iteration with the solution of the fine mesh and calculates the difference $\Delta\phi$ averaged over the whole domain. The result is shown in Figure 4.10. After about 20 iterations there are no changes anymore. Since in the PIC simulation includes almost about 10^7 timesteps in which the solver works, one must not care about these numbers of iterations. They are automatically done in PIC. The larger problem is that the potential converge into a solution that is different to that from the fine grid. The mean difference over the whole domain for the converged solution is $\Delta\phi = 0.043$, which equals about 1% of

the largest value at the anode. The error over the simulated domain is shown in Figure 4.11.
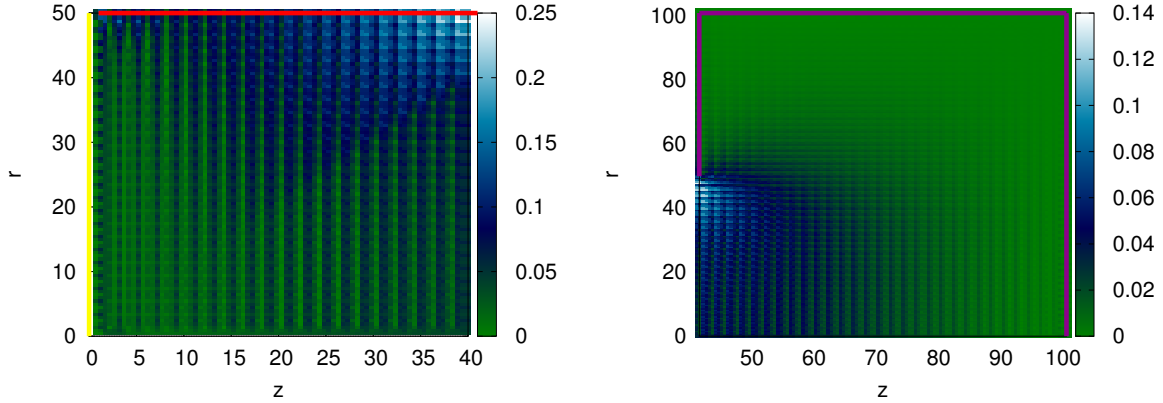
Figure 4.11.: mean error of the converged solution in the channel (left) and in the plume (right) color encoded

In the left part of Figure 4.11 one sees that the largest error in this part of the domain occurs at the upper right border. Since the potential there is mostly driven by the boundary condition of the grounded metal cells at the right end of the dielectrics, this is not surprising. From there on the cells with larger error seem to be orientated towards the dielectrics. The plume region shows a similar behavior with the largest error again at the grounded cells right-side of the dielectrics. With the iterative splitting method one converges during the iterations into a different solution as with the fine mesh, whereas the method with one matrix gives a similar one. Physically the differences of both solutions are very small ($< 1\%$) and can therefore be neglected.

4.2.3. Successive Over-Relaxation

Until now different algorithms to calculate the discretization matrix have been presented. In the following alternatives for the LU decomposition to solve the system of equations will be shown, since for large 3D systems a LU decomposition including the backsolve will be too costly in terms of numerics [13]. One hopefully finds possibilities, which are easier to parallelize than the backsolve of SuperLU. The iterative character of the method is described by its name Successive Over-Relaxation (SOR). According to [14] the principle of SOR is given by

$$\phi^{n+1} = \omega\phi^* + (1 - \omega)\phi^n = \phi^n + \omega(\phi^* - \phi^n) \qquad . \tag{4.2.2}$$

The super-scripted variables define the timestep the potential value is taken from. ω is the relaxation parameter. In general $\omega > 1$ (over-relaxation) speeds-up the process of converging, whereas $\omega < 1$ (under-relaxation) is used to stabilize the algorithm. ϕ^* is the result of a certain numerical method. Two of them will be presented and tested in the following.

Jacobi Method

The Jacobi method is an explicit iterative scheme. In a two-dimensional grid it is defined by

$$\phi_{i,j}^* = \frac{1}{a_{i,j}} \left(a_{i-1,j}\phi_{i-1,j} + a_{i+1,j}\phi_{i+1,j} + a_{i,j-1}\phi_{i,j-1} + a_{i,j+1}\phi_{i,j+1} \right) \qquad . \qquad (4.2.3)$$

So $\phi_{i,j}^*$ is calculated only by values from the timestep before. Due to that this method is perfectly suited for parallelization, every line of the discretization matrix can be distributed to a single processor. The disadvantage is, that many iterations are needed until a solution is converged. This behavior is shown in the left part of Figure 4.12 and is tested for different ω.

One can see, that in accordance to the theoretical prediction a larger ω speeds up the iterative process. Values $\omega > 1$ are not reasonable, since they lead to a divergent solution. This test was done with a domain of 10500 cells without any particles. To study the scaling with different domain sizes different tests were done. They are visualized in the lower right part of Figure 4.12. The difference between iterations needed with higher ω is increased with higher number of cells. For this method $\omega = 1$ is the best choice for this particular case.

Gauss-Seidel Method

In contrast to the Jacobi method the Gauss-Seidel method is implicit. The iterative character is kept. The difference to the Jacobi method is that one uses not only values from the previous timestep, but also values that are already calculated for the current timestep. The underlying equation of the Gauss-Seidel algorithm is given in (4.2.4).

$$\phi_{i,j}^* = \frac{1}{a_{i,j}} \left(a_{i-1,j}\phi_{i-1,j}^{n+1} + a_{i+1,j}\phi_{i+1,j}^{n} + a_{i,j-1}\phi_{i,j-1}^{n+1} + a_{i,j+1}\phi_{i,j+1}^{n} \right) \qquad . \qquad (4.2.4)$$
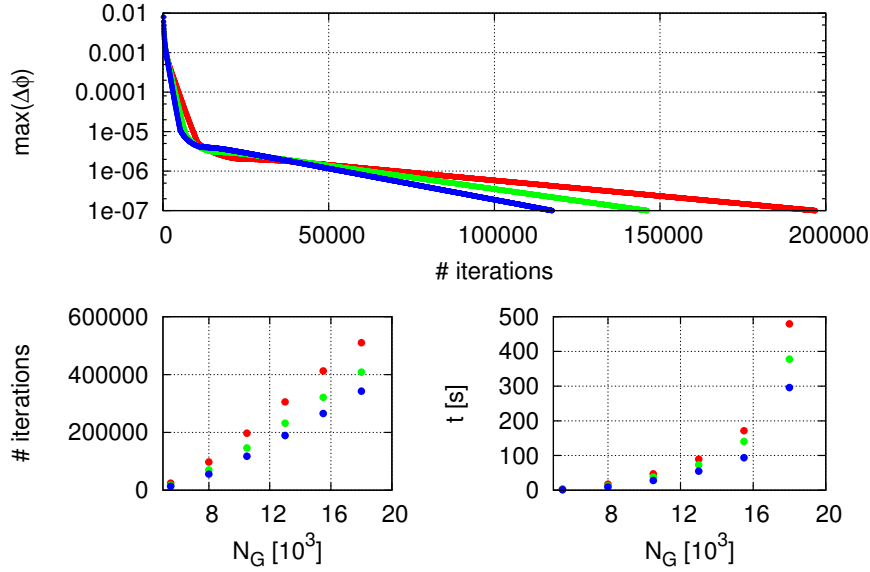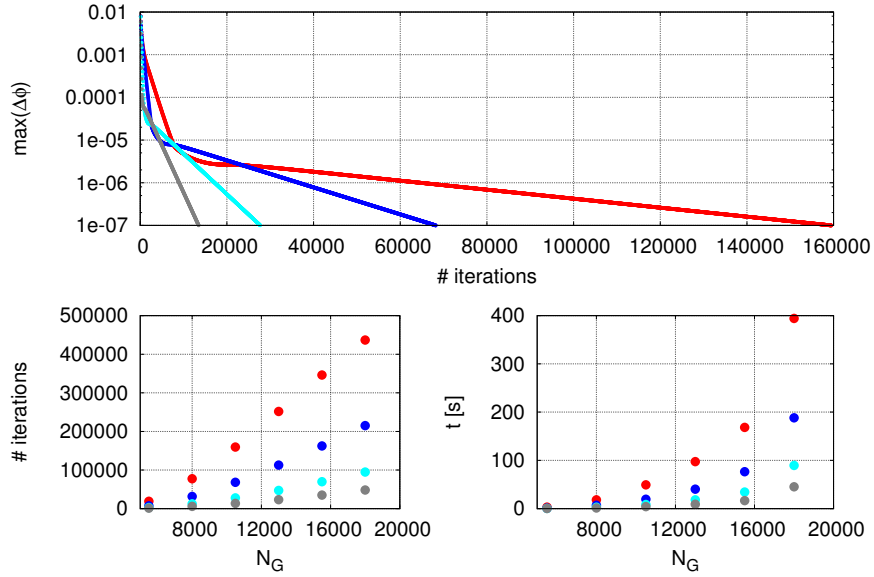
Figure 4.12.: convergence characteristics of the Jacobi method with different SOR
parameter for $N_G = 10500$ (upper plot);
iterations (bottom left) and time (bottom right) needed to reach a con-
vergence of $\Delta\phi < 10^{-7}$ over number of grid cells N_G with the Jacobi
method and different SOR parameter
red $\omega = 0.5$; green $\omega = 0.75$ and blue $\omega = 1$

With the obtained ϕ^* one is again able to calculate ϕ^{n+1} using the SOR equa-
tion (4.2.2). Analog to Figure 4.12 one can make the same tests for the Gauss-Seidel
method and gets Figure 4.13.

Even with the same parameter $\omega = 0.5$ one needs about 40000 iterations less to
reach the convergence criteria $\max(\Delta\phi) < 10^{-7}$. For $\omega = 1$ the difference between
both methods is still larger. One gets a $\max(\Delta\phi) < 10^{-7}$ about 80000 iterations
earlier with the Gauss-Seidel method. Another point of interest is that with the
Jacobi method it is possible to use relaxation parameters $\omega > 1$ which would speeds
up the convergence. With $\omega = 1.75$ the solution is converged after less than 20000
iterations whereas with Jacobi's method one needs a minimum of 100000 iterations
even at the largest ω.

Both methods scale linearly with number of iterations needed to reach a specific
$\Delta\phi$. The quadratic behavior of the required time shown in the lower right plot in
each figure is trivial to understand, because the entries of the matrix are proportional
to the square of the number of grid cells N_G. therefore, it is necessary to think about
other strategies of minimizing the computational time for large cell numbers.

Figure 4.13.: convergence characteristics of the Gauss-Seidel method with different
SOR parameter for $N_G = 10500$ (upper plot);
iterations (bottom left) and time (bottom right) needed to reach a convergence of $\Delta\phi < 10^{-7}$ as a function of number of grid cells N_G with
the Gauss-Seidel method and different SOR parameter
red $\omega = 0.5$; blue $\omega = 1$; cyan $\omega = 1.5$ and gray $\omega = 1.75$

Strategies for Parallelization

Parallelization is one possible approach to speed up the calculation. Although the
Gauss-Seidel method seems very promising in the numerical comparisons until now,
it is very difficult to parallelize. Due to the implicit character it is not so trivial as
for the Jacobi method.

One possible idea for PIC's Poisson solver will be to divide the computational do-
main into several sub-domains, calculate each sub-domain with Gauss-Seidel method
on a single core and only do the matching at the interface between the sub-domains
with Jacobi. To validate this idea, one makes tests with two domains, where different
solver are introduced. Close to the channel one uses the accurate and fast Gauss-
Seidel method, in the plume one implements the Jacobi method. The Gauss-Seidel
method was modified with SOR using the highest possible SOR factor $\omega = 1.75$.
Beginning from a run without the Jacobi method one introduces more and more cells
where Jacobi's method is applied to up to a run where one uses the Jacobi method for
every cell. Figure 4.14 shows how many iterations are needed to reach convergence
as a function of the number of cells with the Jacobi method. For this test a grid with

33000 cells and one with 50500 cells are used.
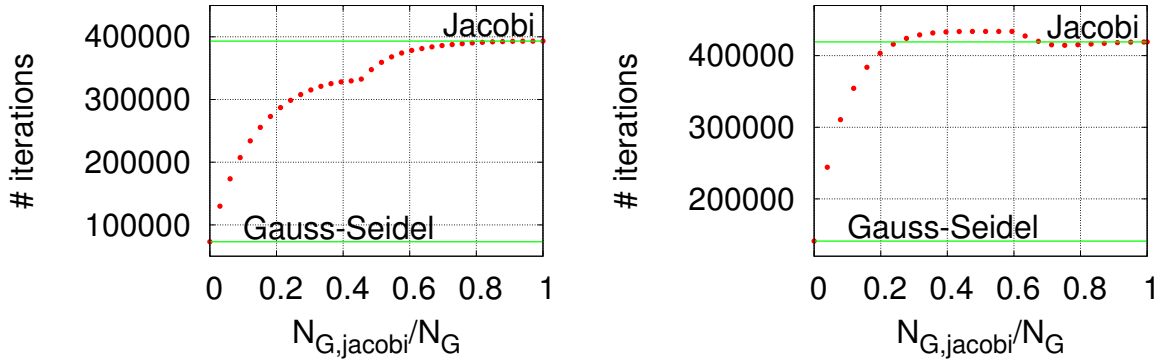
Figure 4.14.: number of iterations to reach numerical convergence as a function of percentage of Jacobi cells for $N_G = 33000$ (left) and $N_G = 50500$ (right)

Even with a small Jacobi region one needs much more iterations than with pure Gauss-Seidel method. Therefore, one has to carefully check, whether this option is good to use for parallelizing the PIC solver. The convergence seems to be strongly coupled to the slowest method which was used and therefore is orientated on the Jacobi method with its slow convergence. Even with a few cells where the Jacobi method is used the convergence is much slower than with a pure Gauss-Seidel domain. Interesting is the different behavior for the two grids. While with $N_G = 33000$ cells one has a continuous increase of needed iterations, for $N_G = 50500$ cells has a maximum between 40% and 60% and decreases then to the pure Jacobi solution. Even for a few cells using the Jacobi method, the convergence is slowed down.

Reconverging after a small Perturbation

More important than finding an initial solution is the reaction to a small perturbation. In other words one will check, how fast a solution reconverges in both methods if one takes a converged solution and adds a small oscillation of only few Volts. For these tests, that are closely connected to the PIC application one distinguishes between numerical and physical convergence. In the following numerical convergence means $\Delta\phi < 10^{-7}$. Important is to analyze the reaction to different amplitudes of the added signals.

At first the goal should be to reach numerical convergence with both methods. The result is shown in Figure 4.15.

All these test are done on a grid of 10500 cells. Obviously, the Gauss-Seidel method is faster than the Jacobi method. The SOR factor $\omega = 1.75$ gives an extra speed up.
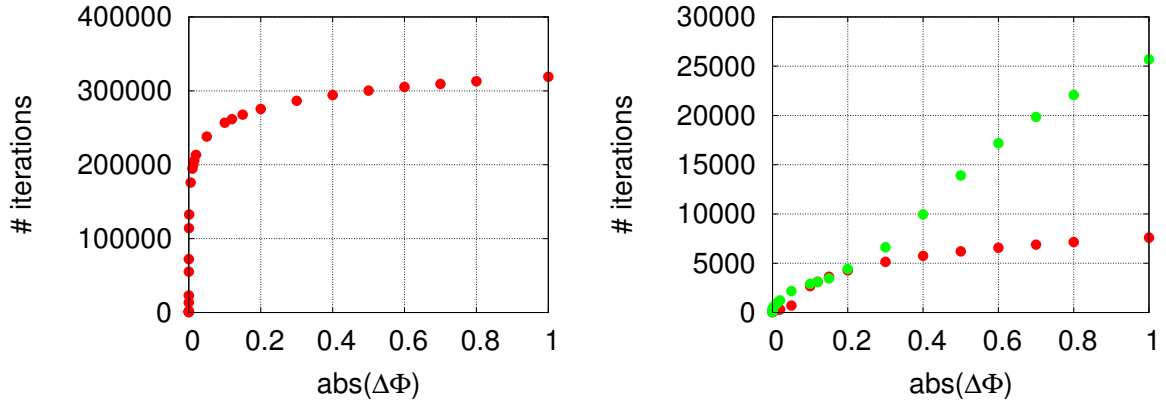
Figure 4.15.: needed number of iterations to reconverge after adding a small perturbation $\Delta\Phi$ to a already converged solution with the Jacobi method (left), the Gauss-Seidel method (right with green dots) and Gauss-Seidel with a SOR factor of $\omega = 1,75$ (right with red dots)

There is one more difference that is not directly clear from Figure 4.15 itself. These tests are done with an initial solution that is already converged. To reach this converged solution from scratch with Jacobi method one needs 117518 iterations. So using this solution and adding an oscillation makes it much harder for the algorithm to reconverge. For an amplitude of $\Delta\Phi = 0.5$ one needs about three times the number of iterations, so probably it would be easier to start from scratch in every step, which is not convenient for the PIC algorithm.

The behavior of the Gauss-Seidel method depends on the different SOR factors. With a SOR factor of 1 one needs 68209 iterations to converge from the scratch to the vacuum solution and with $\omega = 1.75$ still 13491. Compared with the number of iterations Figure 4.15 these are much lower, so with an already converged solution it is easier to reconverge after a perturbation. This can probably be explained by the implicit characteristics of the Gauss-Seidel method.

After this test one has to check the same behavior for physical convergence. Physical convergence means in this context for a physical solution and with physical parameters not an accuracy of $\Delta\phi < 10^{-7}$ is needed. Therefore as mentioned before one uses $\Delta\phi < 10^{-3}$. This results in the plot shown in Figure 4.16.

Because with 10500 cells one converges even with the Jacobi method too fast to compare it, for the test of physical convergence the grid was enlarged to 45500 cells. Even with this larger grid one needs much less iterations to converge. Both methods are similar at that point. Interesting is that with Gauss-Seidel there is a range $|(\Delta\phi)| \in [0; 0.4]$ where the Gauss-Seidel method without SOR is faster than with a
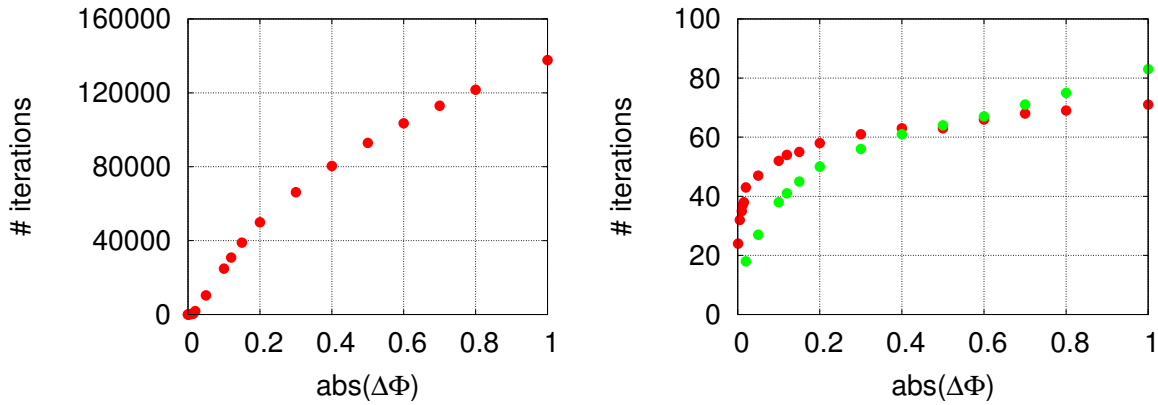
Figure 4.16.: needed number of iterations to reconverge in a physical sense after adding a small perturbation $\Delta\phi$ to a already converged solution with the Jacobi method (left), the Gauss-Seidel method (right with green dots) and Gauss-Seidel with a SOR factor of $\omega = 1.75$ (right with red dots)

SOR factor of 1.75.

At this point one should mention again, that the Gauss-Seidel method can not be parallelize trivially. Hence it is not well suited as an alternative for the one grid approach for 3D PIC, although of its numerous advantages in terms of numerical characteristics. To avoid this bottleneck one can make domain decomposition and calculate every domain with the Gauss-Seidel method on a single core and only do the matching between the cores with the Jacobi method, so a parallelization is possible, but not as trivial as with the Jacobi method. The question is what will be more promising for the application in PIC. Due to the large advantages of the one grid approach it is chosen to make some physical tests in the next section.

4.3. Physics Validation Tests

4.3.1. Uniformly Charged Ring

After doing numerical tests to decide which method to use for the Poisson solver, as a physicist one is interested in correct physical behavior of the solver. Therefore one must benchmark the numerical solution with an analytic one. A first system which is known from literature is the potential of a uniformly charged ring presented in Figure 4.17:

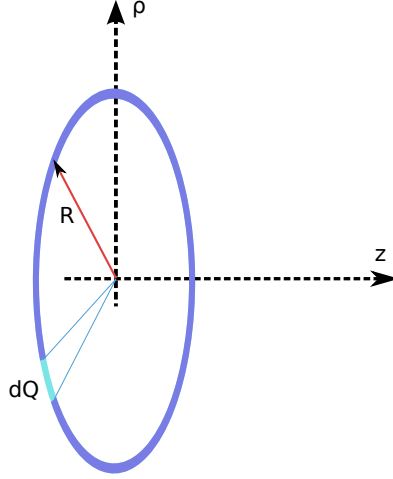Nearly every student of physics has solved this problem for some special cases like

Figure 4.17.: system of a charged ring

the center of the ring. Finding a complete analytic solution was an open question only recently solved. Ciftja et al. have found a way to solve this problem analytically [15]. They derived the following form of the potential Φ:

$$\Phi(\rho, z) = \frac{k_e Q}{\sqrt{(\rho + R)^2 + z^2}} \frac{2}{\pi} K \left[\frac{4\rho R}{(\rho + R)^2 + z^2} \right] \tag{4.3.1}$$

where k_e is Coulomb's electric constant. K is the complete elliptic integral of first kind, which is given by:

$$K(m) = \int_0^\pi \frac{\mathrm{d}\theta}{\sqrt{1 - m \sin^2(\theta)}} \qquad . \tag{4.3.2}$$

The analytic solution can be calculated and will be compared with the numerical solution of the Poisson solver. For the developed axis symmetric Poisson solver one can easily simulate this system by initializing one cell at $\rho = R = 100\,\mathrm{m}$ with the charge $Q = 10^7 e$ where e is the elementary charge. Due to the rotational symmetry this will be exactly the same as an uniformly charged ring. The comparison of the analytic solution and the numerical output of the solver is shown in Figure 4.18.

One can see that the solution is very accurate and close to the analytic one. As an addition one can also compare the electric field calculated numerically and analytically. Due to the symmetry of the system the z-component of the electric field will vanish. Therefore, one has to calculate only the derivative with respect to ρ:

$$\vec{E} = -\vec{\nabla}\Phi(\rho, z) = E_\rho \vec{e}_\rho = \frac{\partial \Phi}{\partial \rho} \qquad . \tag{4.3.3}$$
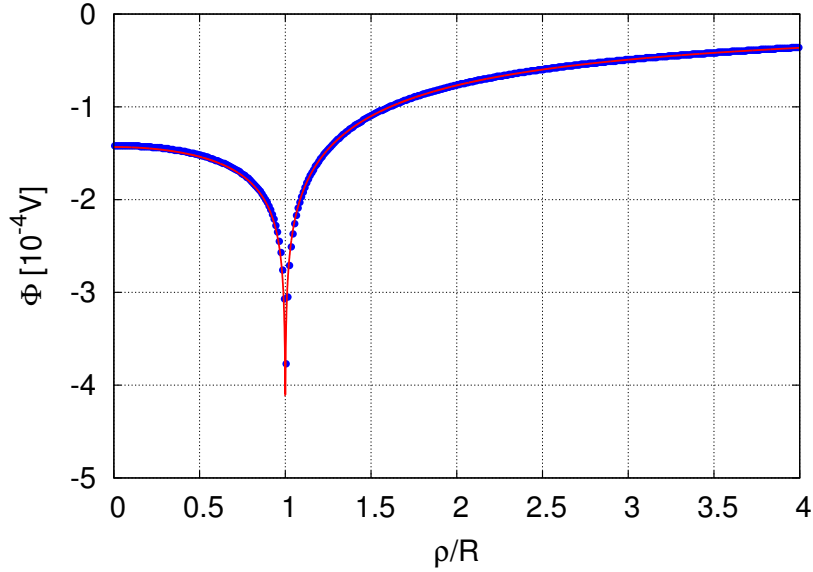
44

Figure 4.18.: comparison of analytic (red line) and numerical (blue dots) solution of the potential of a uniformly charged ring

Using the product rule for differentiation one gets:

$$
-\frac{\partial \Phi}{\partial \rho} = -\frac{2k_e Q}{\pi} \left\{ \frac{\partial}{\partial \rho} \left(\frac{1}{\sqrt{(\rho + R)^2 + z^2}} \right) K \left[\frac{4\rho R}{(\rho + R)^2 + z^2} \right] \right.
$$
$$
\left. + \frac{1}{\sqrt{(\rho + R)^2 + z^2}} \frac{\partial}{\partial \rho} \left(K \left[\frac{4\rho R}{(\rho + R)^2 + z^2} \right] \right) \right\} \quad . \tag{4.3.4}
$$

The largest problem is to find the derivative for the elliptic integral K. According to [16] one can use the low-order differentiation:

$$
\frac{\partial K(m)}{\partial m} = \frac{E(m)}{2(1 - m)m} - \frac{K(m)}{2m} \tag{4.3.5}
$$

with $E(m)$ as an other complete elliptic integral of second kind, which is defined as:

$$
E(m) = \int_0^{\pi/2} \sqrt{1 - m \sin^2(\theta)} \, d\theta \quad . \tag{4.3.6}
$$

One can substitute $m = \frac{4\rho R}{(\rho + R)^2 + z^2}$ and get the following result:

45

$$E_\rho = - k_e Q \frac{2}{\pi} \Bigg[- \frac{\rho + R}{((\rho + R)^2 + z^2)^{3/2}} K(m)$$
$$+ \frac{1}{\sqrt{(\rho + R)^2 + z^2}} \left(\frac{4R}{(\rho + R)^2 + z^2} - \frac{8\rho R(\rho + R)}{((\rho + R)^2 + z^2)^2} \right) \left(\frac{E(m)}{2(1 - m)m} - \frac{K(m)}{2m} \right) \Bigg] \quad .$$
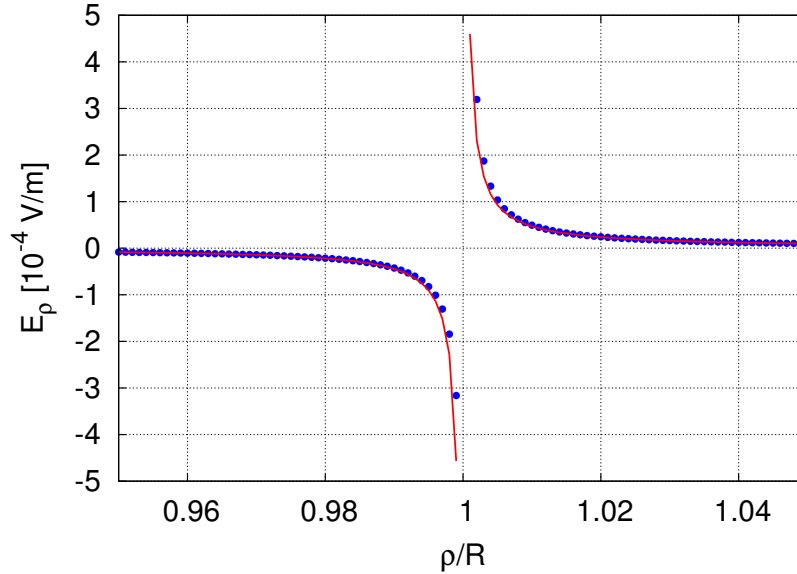$$(4.3.7)$$

Figure 4.19.: comparison of the analytically (red line) and numerically (blue dots) calculated ρ-component of the electric field for a uniformly charged ring

Again one can compare the analytic solution for the electric field with the numerical one. The result is shown in Figure 4.19. As expected from the potential also numerical and analytic solution of the electric field are in good agreement. There are only minor deviations due to numerical accuracy around the divergence at $\rho = R$.

4.3.2. Uniformly Charged Infinite Cylinder

Another system with known analytic solution is a uniformly charged infinite cylinder. This is used as benchmark for the axis-symmetric Poisson solver. The setup is shown in Figure 4.20.

The analytic solution of such a system is well-known. One can derive it easily applying Gauss's law:
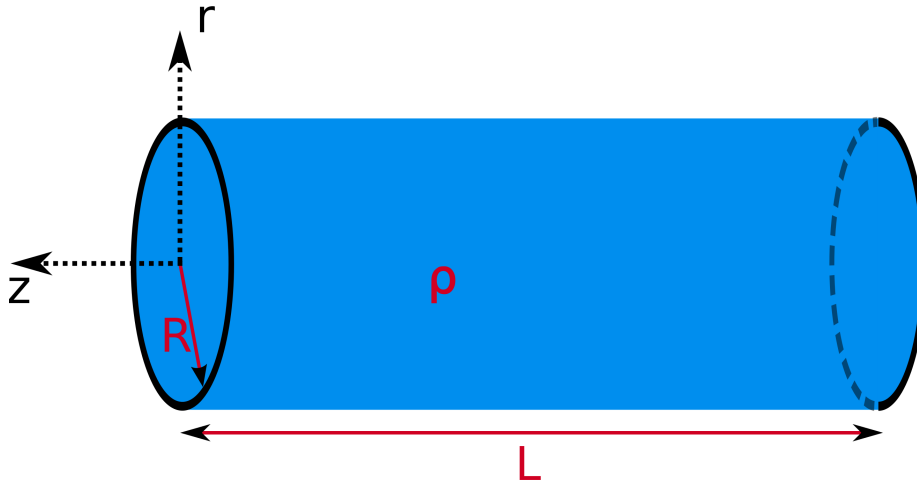
Figure 4.20.: scheme of a charged cylinder

$$\int \nabla \vec{E} \mathrm{d}V = \oint \vec{E} \mathrm{d}A = \int \frac{\rho}{\epsilon_0} \mathrm{d}V = \frac{Q}{\epsilon_0} \qquad (4.3.8)$$

where ρ is the charge density and ϵ_0 the vacuum permittivity. The integration can be done trivially:

$$E \cdot A = E \cdot 2\pi r L = \frac{Q}{\epsilon_0} = \frac{\rho \pi r^2 L}{\epsilon_0} \qquad \text{for} \quad r < R \qquad , \qquad (4.3.9)$$

$$E \cdot A = E \cdot 2\pi r L = \frac{Q}{\epsilon_0} = \frac{\rho \pi R^2 L}{\epsilon_0} \qquad \text{for} \quad r \geq R \qquad , \qquad (4.3.10)$$

with L as the length, which is defined to express the surface A, and R the radius of the cylinder. Finally the electric field is given as

$$E(r) = \frac{\rho r}{2\epsilon_0} \qquad \text{for} \quad r < R \qquad , \qquad (4.3.11)$$

$$E(r) = \frac{\rho R^2}{2\epsilon_0 r} \qquad \text{for} \quad r \geq R \qquad . \qquad (4.3.12)$$

Inside the cylinder one gets a linear increase of the absolute value of the electric field with radius and outside the cylinder the strength of the electric field decreases with $\frac{1}{r}$. This behavior is visualized in Figure 4.21 for $Q = 10^7 e$. The radius is set to $R = 100\,\mathrm{m}$.

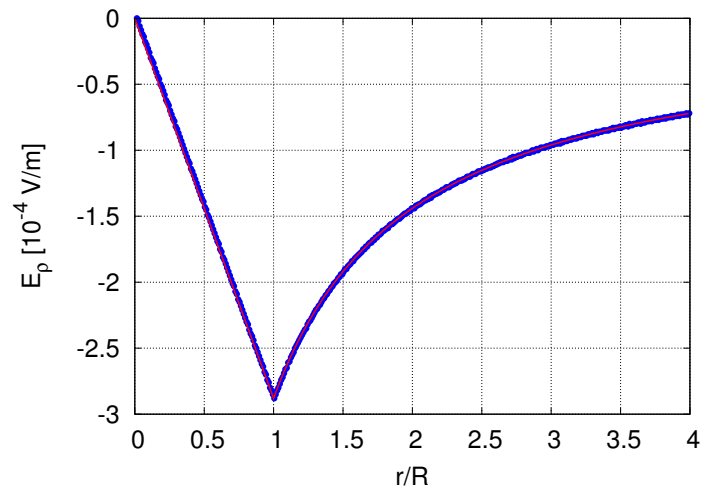Obviously the analytic and the numerical solution are in very good agreement.

Figure 4.21.: comparison of the analytically (red line) and numerically (blue dots) calculated ρ-component of the electric field for a uniformly charged cylinder

Summarizing the results from the physical and the numerical tests the one grid approach is the best choice for the Poisson solver in two axial-symmetric dimensions.

5. Analysis of Thruster Physics

5.1. General Characterization of HEMP-T

In the following chapter a description of the basic physics of an ion thruster will be given for the example of the HEMP thruster. In Figure 5.1 a schematic view of the actual HEMP thruster analyzed in this work is shown. In difference to Figure 2.6 a thruster with only one inner cusp is used. There are several models of the HEMP thruster existing, details can be found in [17].

Patented, simplified principle of the cylindrical
HEMP thruster with PPM focusing system

U ~ 300V to 2000V

Cathode neutralizer emits electrons required for discharge ignition and ion beam neutralisation

S N N S

Anode

E-Field

E-Field

e⁻

B-Field

B-Field

Xe⁺ ion beam

Xe gas

symmetry axis

electrons on closed drift orbits
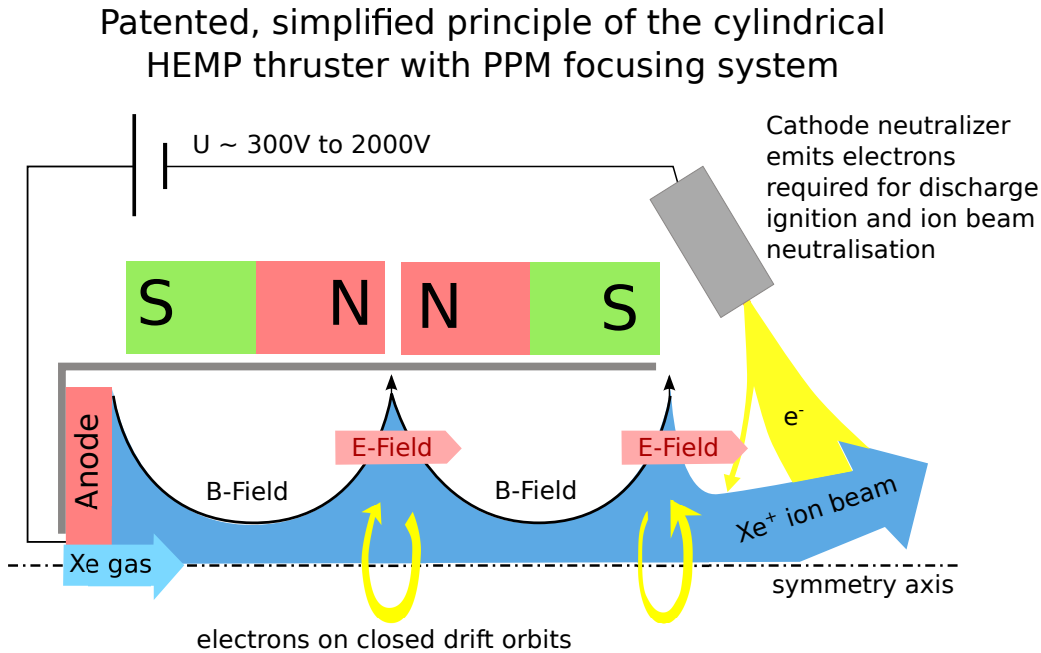
Figure 5.1.: schematic view of the HEMP-T concept

The HEMP thruster has a dielectric, rotationally symmetric discharge channel with an anode, located at the upstream end. In the discharge channel the electrons accelerated by the anode create ions by ionization of neutrals used as propellant. At the downstream end of the discharge channel the thruster exit is located. Outside the thruster, behind the thruster exit, a hollow cathode neutralizer provides electrons to

avoid charging of the satellite by compensating the outstreaming ions. This electron source also acts as primary source of electrons for the thruster plasma.

Radially, the channel is limited by a dielectric ring followed by a system of axially magnetized permanent magnet rings. The magnets are positioned with alternating magnetization, which means that identical poles of the magnets face each other. In these regions between the magnets so-called cusps are created. They can be characterized as regions with perpendicular magnetic field lines towards the wall. The magnetic field topology changes between areas with dominant axial or radial magnetic field. The strength of the magnetic field is chosen such that electrons are magnetized and follow magnetic field lines. That means that the Larmor radii of electrons are much smaller than the system length. The typical length of the discharge channel is about 5 cm, the radius is about 1 cm. Electrons are guided into the magnetic cusps, where they are trapped.

To understand such trapping of electrons, one has to understand the principle of a magnetic mirror. Magnetic field lines are getting closer within the cusps. The velocity of the electrons decreases with the density of the field lines so that they even can get reflected [18]. In general a magnetic mirror reflected charged particles from a magnetic field region with denser magnetic field lines. As an electron gyrates along a magnetic field line and enters a region of denser field lines, the azimuthal motion of the electron and the radial component of the magnetic field, results in a Lorentz force pointed away from the strong field region. This force can reflect the electron. In thrusters magnetic field lines are squeezed close to the cusps and generate a magnetic mirror. This magnetic mirror acts only on electrons, because ions have a much higher mass and their Larmor radius exceeds the system length of the thruster. Ions are non-magnetized, but are coupled within the plasma to the movements of electrons by the request of quasi-neutrality on the length scale of the Debye length.

The transport of electrons perpendicular to the magnetic field lines, towards the anode cusp is caused by anomalous diffusion. Electrons, which are emitted by the neutralizer, are trapped in the magnetic cusp close to the exit of the discharge channel. The confined electrons in the exit cusp pull down the potential at the exit. Due to this potential drop the ions are accelerated as there is a virtual grid. Since the radial magnetic field is very strong at the exit away from the axis, most of the electrons are not able to enter the channel. Only some of them will overcome this barrier due to collisions or anomalous transport. In addition, electrons close to the channel axis are able to enter due to the dominant axial field in this region. Electrons getting

into the channel have very large kinetic energies when they are accelerated in the potential drop at the exit cusp. High energy electrons lead to a stronger ionization of the neutral propellant gas, especially in the next upstream cusp, where most of these electrons are trapped. Electrons in the cusps region have a long residence time there due to the mirror trapping and increase by this the ionization probabilities. Between the cusps the dominant axial field will lead to a rather homogeneous filling. The competition of radial transport including classical collisions and anomalous transport, specifically important to allow electrons to overcome the cusps, and axial transport in particular close to the axis determines the plasma potential. Their relative strength decides if the cusps get strongly visible as steep steps (in the case of very strong radial transport) or as only weak perturbations (in the case of dominant axial transport) with an additional steep gradient at the exit, where ions are accelerated. Numerical analysis [11] using a 2-dimensional axis-symmetric PIC code demonstrated that a rather smooth potential profile with only weak signatures of the cusps establishes very similar to potentials of grid thrusters. 3D studies demonstrated that for HEMP-T anomalous electron transport via electrostatic turbulence is limited mostly to the cusp region due to the strong radial magnetic field. In contrast to this common Hall thruster where the radial magnetic field is much stronger are much more dominated by turbulence. Therefore, HEMP-T classical collision processes are quite important allowing a more robust prediction by modeling as turbulence-dominated Hall thrusters.

For the potential, the following boundary conditions are used: an anode voltage of $500\,\mathrm{V}$, $E = 0$ at the end of the domain in z-direction and $\Phi = 0$ at the end of the domain in r. In contrast to many other simulations the dielectric is not implemented as a local boundary condition [19]. The formulation of finite volumes guarantees the correct physical implementation, that the normal component of the electric field perpendicular to the dielectric surface (namely in radial direction) has to be identical at the interface. This treatment guarantees a fully self-consistent of the potential in the whole domain and to resolve the floating potential at the dielectric surfaces including non-local effects neglected in the standard cloaca implementation of local boundary conditions at the dielectric surface. A converged PIC-run in quasi steady state is used to calculate it after 6×10^6 timesteps.

For the HEMP thruster the potential is shown in Figure 5.2 In the plasma bulk it is nearly constant with a steep drop at the thruster exit producing a high thrust. Close to the axis the mainly axial magnetic field allows the electrons to flow parallel
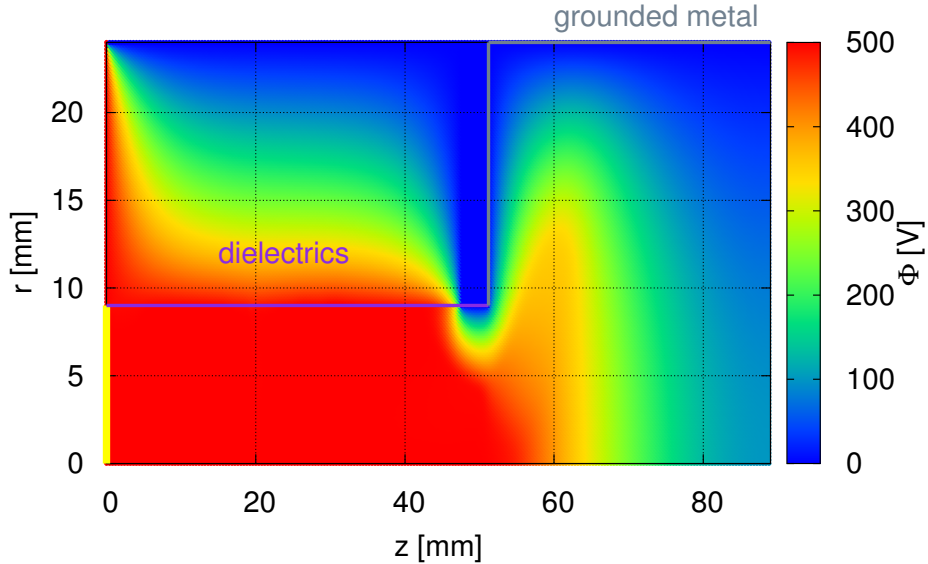
Figure 5.2.: potential of a HEMP thruster

to the electric field. A small perturbation of the electric potential is therefore quickly compensated by fast electrons. The potential in the plasma bulk is nearly constant and equal to the anode voltage over the whole channel. It results in a steep drop at the thruster exit, producing a high thrust. Here the mainly axial magnetic field allows the electrons to flow in parallel to the electric field. A small perturbation of the electric potential is therefore quickly compensated by fast electrons. The radial and axial strength of the drop at the exit is the reason for the acceleration of ions and defines their angular distributions. High energy ions are only generated close to the exit cusp of the thruster. Close to the thruster walls, the potential decreases due to the boundary condition of zero net current at the wall. In the cusp region at about $z = 19mm$, the potential is dropping smoothly due to the radial $\vec{B}$ field.

5.2. Velocity Distribution Function Characteristics

To characterize the basic physics of HEMP-T a diagnostic tool is implemented in the PIC code to calculate the velocity distribution functions with spatial resolution over the whole domain for all species. All velocity distribution functions (Figure 5.4, 5.7 and 5.10) are temporally averaged over 10^6 timesteps of a quasi steady-state run. All particles with $r < R_{thruster} = 9\,\text{mm}$ are taken into account, that means velocity distribution functions spatially averaged over the acceleration channel are calculated. Plots 5.3 and 5.6 show the density for electrons and ions after $6 \cdot 10^6$ timesteps of the

same run. They can be seen as snap-shots at this time.

5.2.1. Electrons

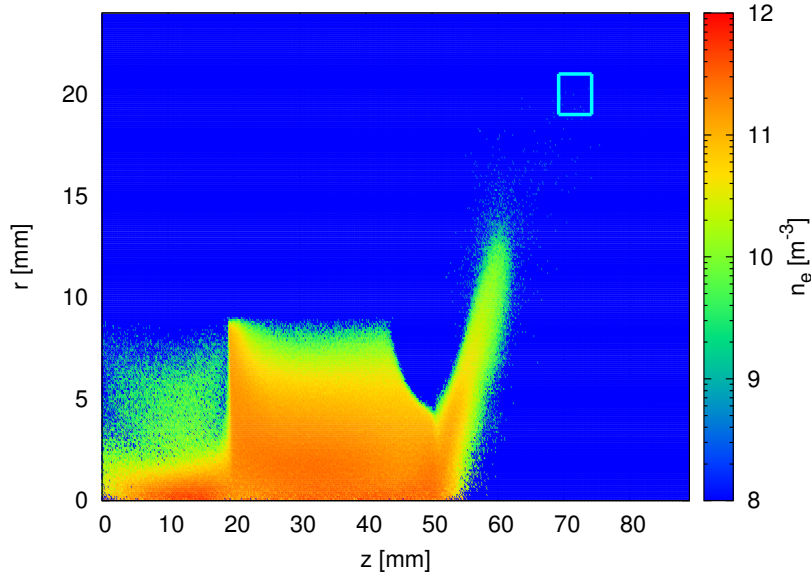The electron density distribution is shown in Figure 5.3.

Figure 5.3.: density profile for electrons for a HEMP thruster, the light blue marked region in the plume represents the cathode neutralizer

The influence of the plasma sheath can also be seen in the electron density presented in Figure 5.3. The electron density is uniformly decreasing towards the channel walls and the cusp region is clearly visible. The higher electron density in this region due to magnetic mirroring at the denser magnetic field lines is visible.

It is also visible that the density is strongly decreasing after the exit in the plume region with the exception in the direction of the primary source of electrons at the neutralizer. At $z = 70\,\text{mm}$ the density is decreased by at least 4 orders of magnitude compared to the channel. The region between the inner cusp and the exit cusp has a higher electron density than the region between anode and the inner cusp. This means that the transport of electrons from the neutralizer entering the channel after passing the exit cusp is larger than through the second cusp. The wall contact of the electrons is limited to the cusp regions. Only electrons from the neutralizer are in the plume with velocities directed towards the channel, because the source electrons are accelerated by the potential in this direction. In Figure 5.4 the velocity distribution function is plotted.
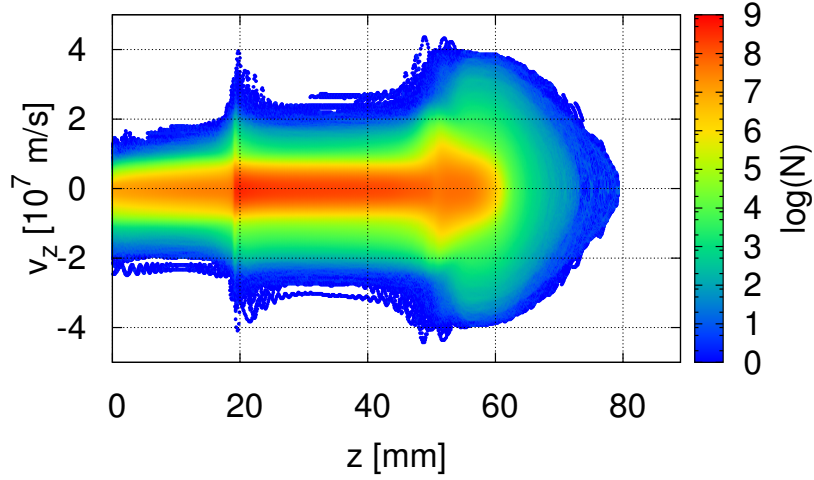
Figure 5.4.: electron axial velocity distribution function for $r < R_{thruster}$ as a function of the axial position z

For all z the distributions look rather symmetric in velocity space on this scale. This can be understood by the relative small average energies of the electrons of about several eVs. Analyzing the distribution functions further in detail cuts through the profile are shown in Figure 5.5.
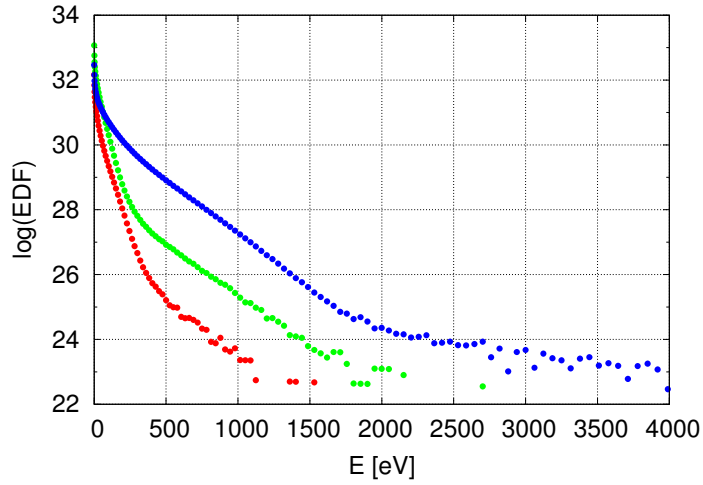

Figure 5.5.: electron energy distribution function at different axial positions $10\,\mathrm{mm}$ (red), $35\,\mathrm{mm}$ (green) and $51\,\mathrm{mm}$ (blue)

In this logarithmic scale a Maxwellian distribution function would show a linear dependency. Obviously this is not the case here, since especially at high energies there are particles that would not be represented in a Maxwellian distribution function. So in the channel they are essentially non-Maxwellian, which means that the mean free paths of electrons are too long to be able to maxwellize the electron distribution

function. This can be proven by simple estimates of mean free path length scales in the channel of the thruster. The smallest mean free path length exists for charge-exchange collisions. All other mean free path lengths are much longer especially the mean free path length for elastic collisions or for excitation.

$$\lambda_{mfp,CX} = \frac{v_n}{\langle \sigma_{CX} v_{ion} \rangle n_n} \qquad . \tag{5.2.1}$$

With v_n and v_{ion} as the velocities of neutrals and ions, which can be evaluated with the assumption of a Maxwell distribution of the temperatures in the channel. Although this is not correct, it will be sufficient for an estimate. Due to very strong coupling of ions and neutrals by charge-exchange collisions both have the similar temperatures in the channel. Therefore, the velocities of neutrals and ions cancel out each other. The neutral density is about $5 \cdot 10^{19} \mathrm{m}^{-3}$. The cross section for charge-exchange reactions for a Xenon gas is can be calculated according to [20]. Therefore one gets gure

$$\lambda_{mfp,CX} \approx \frac{1}{1.57 \cdot 10^{-14} \mathrm{cm}^2 \cdot 5 \cdot 10^{13} \mathrm{cm}^{-3}} \approx 1.2 \,\mathrm{cm} \qquad . \tag{5.2.2}$$

This is the smallest collision length scale in this plasma. Because it is larger than the domain size, the plasma in the thruster is nearly collisionless. Therefore, the plasma has no chance to equilibrate and one should avoid the assumption of a Maxwellian energy distribution. As a consequence, one is not allowed to use fluid equations to describe the physics in the plume correctly. The axial velocity distribution function is much broader in the region about $z = 20 \,\mathrm{mm}$ and $z = 51 \,\mathrm{mm}$, since electrons are strongly heated in the cusps, so in this regions there are more fast particles than in all other regions. Comparing both cusps with each other, the inner cusp is much stronger so that the increase is velocity is very strong at $z = 19 \,\mathrm{mm}$. Outside the cusps the velocity distributions are nearly identical within the channel.

5.2.2. Ions

Due to quasi-neutrality the ions have a similar density distribution in the channel as the electrons. In the first half of the thruster before the inner cusp only near the cusp itself high densities are detectable, whereas the region between inner cusp and exit cusp has a higher density.

As one of the most important features of HEMP-T the wall contact of energetic ions is limited to the cusp region being coupled to the flows of electrons. This can be seen
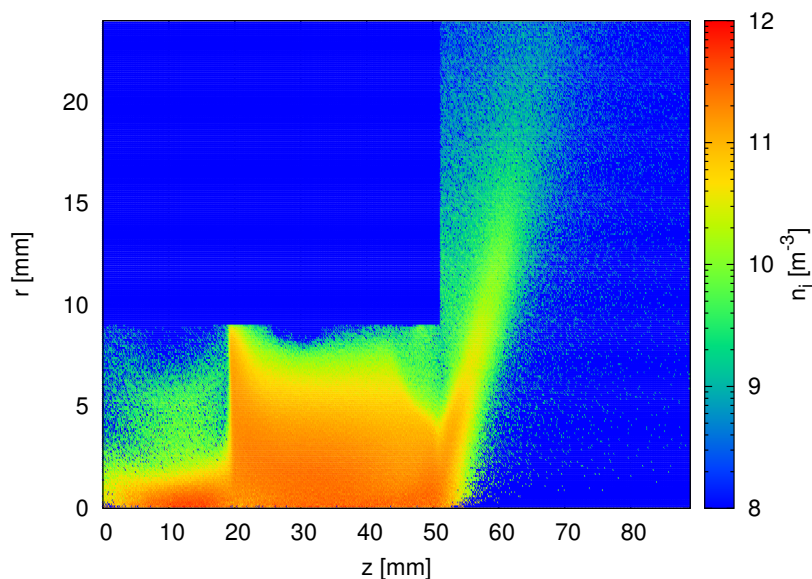
Figure 5.6.: density profile for ions for a HEMP thruster

in Figure 5.6. In the plume the largest disagreement of simulation and experiment appears clearly. As already mentioned in the beginning of this chapter the angular distribution is not in good agreement with experimental results. The reason for more ions in the larger angles as observed in the simulation is that most of the ions leave the thruster with very large radial velocities. One possibility to reduce this effect is to reduce the impact of the boundary conditions affecting this strongly, especially in r-direction. The ion distribution function of the axial velocity is shown in Figure 5.7.
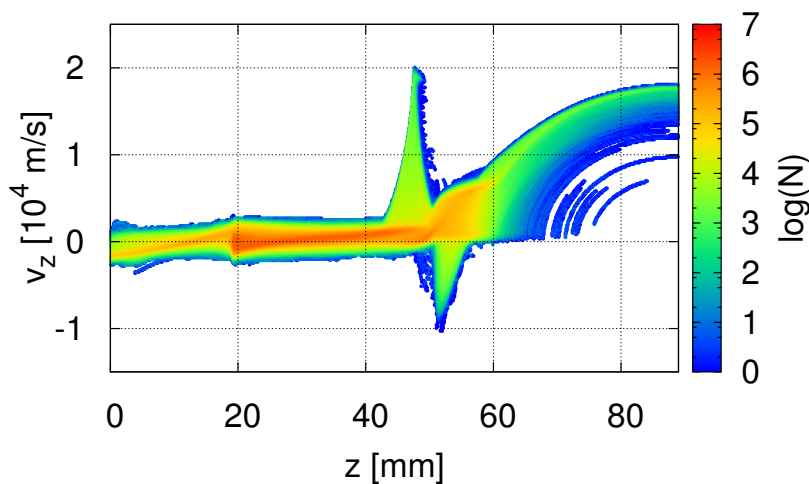
Figure 5.7.: ion axial velocity distribution function with $r < R_{thruster}$ as a function of the axial position z

Within the channel all ions have rather low velocities. They are not accelerated

strongly due to the nearly constant potential profile. Only at the exit they are accelerated by the strong potential drop. Near the exit cusp and in the plume ions with high energies exist.

The first peak in the distribution at $z = 48 \, mm$ with velocities up to $20\,000 \, m/s$ can be explained by the grounded wall after the dielectrics. The grounded metal fixes the potential at $\Phi = 0 \, V$ and ions are accelerated very strong in this direction. The right side of the peak is very steep and leads to a region with large positive velocities. Therefore, these particles loose energy flying in z-direction. This is a direct consequence of the potential structure in this region as shown in Figure 5.2, because after the grounded wall the potential rises again and ions are slowed down by the counter-acting electric field. There is one part of the ion distribution with large negative velocities at $z = 51 \, mm$. Here, ions are accelerated by the potential structure close to the grounded plate in negative direction.

Close to the exit cusp inside the channel there are many ions with low velocities. At the exit cusp and afterwards they are accelerated, seen by the shift of the orange color to higher velocities. This acceleration is a consequence of the steep potential drop at the exit. In this acceleration region the ion density decreases. Most of them fly out of the region used for spatially averaging (namely the channel width) due to their high velocity in radial direction.

Some ions reach the end of the domain with a maximal velocity of about $18\,000 \, m/s$. The velocity of these particles increases up to the end of the domain, since the boundary condition of the potential forces it to decrease up to there. Due to the small plume domain in this run there is no region where both E and Φ are equal to zero and the particles are accelerated in the whole plume region. This explains the trend to higher velocities in Figure 5.7 beginning at the exit cusp at $51 \, mm$ up to the end of the domain. This structure looks like a quarter of a circle in the velocity distribution function. This is analogue to a motion with constant acceleration, where the velocity is proportional to the square-root of the displacement.

As mentioned the exit cusp with its strong potential drop is responsible for the angular distribution of the accelerated ions. In addition, ions are also scattered into the side part of the plume by charge-exchange collisions, where so called wings can build up. These wings are also visible in the ion density profile. This was already measured in the early 1980s by M.R. Carruth Jr. and M.E. Brady [21]. They determined that these wings are part of the charge-exchange plasma flow and may flow back to the spacecraft.

5. Analysis of Thruster Physics

The slow source neutrals, that are injected and not ionized in the channel, can exchange their charge with fast ions during collisions and by this produce slow ions and fast neutrals:

$$\mathrm{Xe} + \mathrm{Xe}^+ \rightarrow \mathrm{Xe}^+ + \mathrm{Xe} \qquad . \qquad (5.2.3)$$

These fast neutrals and fast ions at large angles flowing towards the spacecraft can create damage from sputtering. In the past the region of the plume was mostly studied with hybrid models. These hybrid codes are used to describe the behavior of plasma particles in the plume. Such simulations show the creation of distinguished side wings.

Figure 5.8.: equipotential lines of an SPT-100 in the outer plume [22]

They can be seen as regions beside the actual beam region in Figure 5.8. This plot was calculated from Taccogna et al. [22] using a two-dimensional axis-symmetric hybrid code. In their simulation a particle method for ions and a fluid model for the electrons were applied. The simulated domain has a size of $1.5\,\mathrm{m}$ in axial direction and $1.2\,\mathrm{m}$ in radial direction. The thruster, which is placed in the left upper corner, is an SPT-100.

5.2.3. Neutrals

The neutrals density distribution is influenced by ionization. The consumption of neutrals in ionization reactions can be seen in Figure 5.9. It shows a neutral profile and the calculated ionization reaction rates for HEMP-T including its near field region. The positions of maximum reaction rates for ionization reactions are identical with the positions of holes in the profile of the neutral density and are at the positions of the cusps, where the electrons are heated increasing ionization.

This profile can be understood using an estimate for the ionization mean free path length in the channel and the plume. One expects a length, which is of the order of the system size or smaller for the channel and much larger in the plume, because there are no reactions detected.
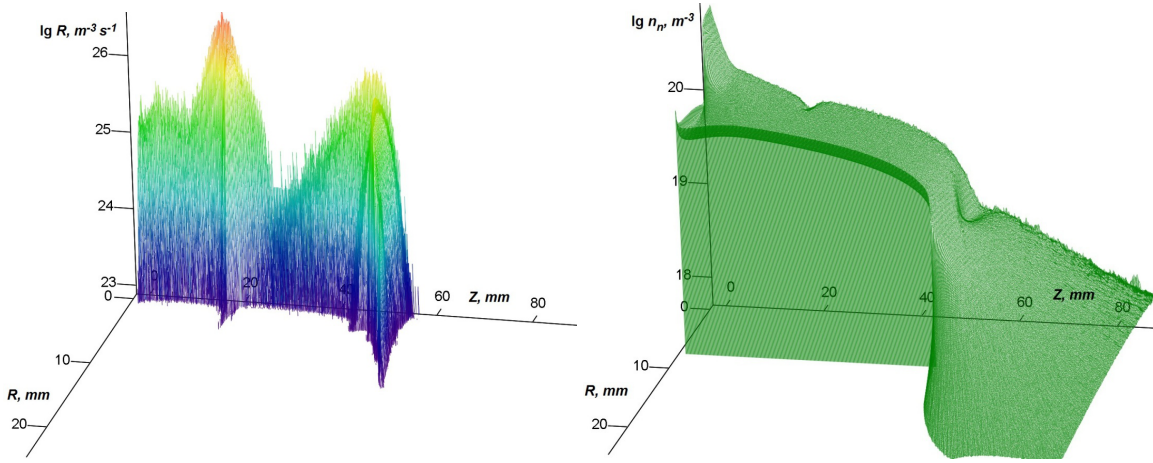
Figure 5.9.: electron impact ionization rate (left) and neutral density (right) of a HEMP thruster including near-field plume [23]

The estimate is done via an integration over the energy distribution. Like in the calculation before, one uses a Maxwell distribution. Although it is not correct, it gives a simple order of magnitude estimate. For calculating the velocity of the neutrals one uses a temperature of $800\,\mathrm{K}$ which corresponds to $0.069\,\mathrm{eV}$. One gets:

$$
\begin{aligned}
\lambda_{mfp,ion} &= \frac{v_n}{\langle \sigma_{ion} v_e \rangle n_e} = \sqrt{\frac{2 k_B T_n}{m_n}} \frac{1}{\langle \sigma_{ion} v_e \rangle n_e} \\
&= \sqrt{\frac{2\ k_B\ 0.069\,\mathrm{eV} \cdot 11\,605\,\mathrm{K/eV}}{131.293\,\mathrm{u} \cdot 1.661 \cdot 10^{-27}\mathrm{kg/u}}} \cdot \frac{1}{3.4655 \cdot 10^{-9}\mathrm{cm}^3/\mathrm{s} \cdot 5 \cdot 10^{12}\mathrm{cm}^{-3}} \\
&\approx 1.84\,\mathrm{cm} \qquad .
\end{aligned}
\tag{5.2.4}
$$

5. Analysis of Thruster Physics

As expected, this value has the same order as the channel radius and is smaller than the length of the channel. In agreement with the results of the simulation, ionization plays a very important role in the channel. A different result is expected in the plume. There, the density of the electrons is much lower. Velocity of neutrals, the cross section and therefore also the integral over the electron velocity stays the same. Since the electron density is at least four orders of magnitude smaller than the density in the channel, compare Figure 5.3, the mean free path is about this magnitude larger. So it is much larger than the size of the plume itself. As a consequence in the plume ionization has no impact. That was already stated in the left part of Figure 5.9 as there are no ionization reactions in the plume.

The mean free path length for charge-exchange reactions outside the channel can be estimated. It should be smaller than the plume itself to have an impact. Analogous to (5.2.1) one can do this very easy. There are only two differences, the higher ion temperature, which is now approximately $400\,\text{eV}$ and the cross section of charge-exchange collisions of Xenon has changed due to the higher energy of ions.

$$
\begin{aligned}
\lambda_{mfp,CX} &= \frac{v_n}{\langle \sigma_{CX} v_i \rangle n_n} \approx \sqrt{\frac{T_n}{T_i}} \frac{1}{\sigma_{CX} n_n} \\
&= \sqrt{\frac{0.069\,\text{eV}}{400\,\text{eV}}} \frac{1}{3.7271 \cdot 10^{-15}\text{cm}^2 \cdot 10^{19}\text{m}^{-3}} \\
&\approx 0.35\,\text{cm}
\end{aligned}
\tag{5.2.5}
$$

with T_n and T_i for the temperatures of ions and neutrals. The temperature of the neutrals is used similar to (5.2.4). Due to the small lengths and in agreement with the expectations charge-exchange reactions have a strong impact in the plume. It is interesting to study the effects connected with charge-exchange reactions in the wings of the plume, if one can extend the domain and therefore simulate also the outer part. These reactions are especially problematic at the side regions of the plume where ions can flow back to the satellite. They can affect the payload of the satellite since they build up electric fields and disturb diagnostics or communication systems of the satellite. Therefore contamination, sputtering and degradation on components of the spacecraft have to be studied. This will be done later.

In Figure 5.10 the axial velocity distribution function for neutrals is presented. One can see that charge-exchange collisions have a strong impact on the velocity profile of neutrals. It couples the neutrals to the ions and is responsible for similarities in

both distribution functions. All regions of high-velocity particles with positive and negative values in 5.10 can be explained by this.
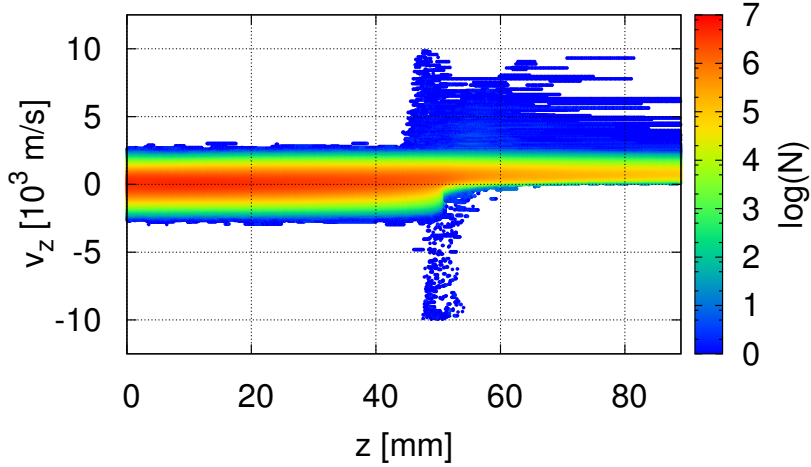

Figure 5.10.: distribution of velocity in axial direction for neutrals for $r < R_{thruster}$

Apart from the high-velocity wings the distribution looks quite more regular, since the neutrals are not affected by the magnetic or electric field. Most of the neutrals have velocities in the range of $-2000\,\mathrm{m/s} \ldots 2000\,\mathrm{m/s}$ and so in the order the ions. The values are equally distributed in positive and in negative direction. This is again a result of the large density in the channel and their relative low temperature. In the plume the situation for neutrals is different. Neutrals are only flying out of the thruster and negative velocities are not detected. If one considers a chamber with uniformly distributed velocities and a hole at one side, particles can flow out only with a positive velocity. This situation is similar to the one in HEMP-T.

Not only time averaged phenomena as discussed before are important to characterize the thruster. There are also dynamic effects, that will be discussed in the following section producing additional instabilities. This is not observed for HEMP-T, therefore Hall thrusters are used for this.

5.2.4. Breathing Mode and Rotating Spoke Instability

In the plasma of a Hall thruster there are several different oscillations in a wide band ranging from $1\,\mathrm{kHz}$ to $20\,\mathrm{GHz}$. One of the slowest and therefore lowest frequency modes is the Hall thruster breathing mode. Although its frequency is very low, it is one of the largest oscillations in Hall effect thrusters. The origin of this oscillation is a "predator-prey" behavior between the ionization-zone and the neutrals in the

thruster channel. It begins with the filling of the channel with neutrals. The Hall current, which has its maximum current density near the peak of the radial magnetic field, starts to ionize these neutrals. If the neutrals are ionized, they will leave back electrons that can contribute to the Hall current. Additional electrons stay in the closed-drift orbits and therefore lead to an increase of the electric field between the anode and the hall current. This increases the $E \times B$-drift and the ionization rate. Enhanced ionization fastly exhausts all neutrals. Afterwards the channel again begins to fill with neutrals and the cycle will be repeated.

If one looks again at Figure 5.9 one can easily explain the breathing mode of such a thruster. At the same time the neutral profile has holes via ionization the neutrals itself are forced to balance these holes with an increased diffusion to these regions. Therefore one gets a continuous periodic behavior of filling up the neutral reservoir in the cusp and again exhaust it due to ionization. The typical time t for this refilling of the holes can be estimated. Therefore one uses a typical velocity of neutrals v_n in the channel and the size of the channel L, because neutrals were not affected by the electric or magnetic field.

$$t = \frac{L}{v_n} \approx \frac{50\,\mathrm{mm}}{100\,\mathrm{m/s}} = 50\,\mathrm{ms} \qquad . \tag{5.2.6}$$

Within this time the neutrals are able to refill the areas of strong ionization and keep the process running. The neutral dynamics is connected to the dynamics of the electrons, because they are responsible for the ionization. A phenomenon which is strongly coupled with the neutral gas depletion is the rotating spoke instability. Its connection to neutral gas depletion due to ionization is well described in [24]. There a fully three-dimensional Particle-in-Cell Monte Carlo Collision model was used to analyze a cylindrical Hall thruster. It was found, that within about $1.2\,\mu\mathrm{s}$ the spoke rotates about $90°$ in the direction of the $E \times B$-drift. The average velocity of the spoke was calculated to $0.8\,\mathrm{cm/\mu s}$, which is about four times higher than laboratory observations. The time how long the neutrals need to refill areas of complete neutral depletion is estimated as $2.2871\,\mu\mathrm{s}$. A still open task is the mechanism of spoke formation and its dynamics including the anomalous transport inside the spoke. One was able to show that the asymmetry caused by the cathode has a huge impact on the spoke. The electron current through the spoke was about $I_e \approx 0.55\,\mathrm{A}$, which is two orders of magnitude higher than the current from classical diffusion processes.

The spoke instability was also of interest for several experimentalists over years. It was firstly observed experimentally in the late 1960s by Janes [25]. They measured

an anomalous electron diffusion, which can not be explained by collisions. In addition they demonstrated that the electron density and plasma potential fluctuations slowly rotate in the $E \times B$ direction. They explained the anomalous transport in the context of rotating density nonuniformities, that become polarized by the electron Hall current. Their experimental data was in reasonable agreement with the theoretical description of Yoshikawa and Rose [26] for anomalous diffusion in a plasma across a magnetic field.

After a phase without any significant investigations, the rotating spoke was again of interest in the Soviet Hall thruster development program Esipchuk in the early 1970s. One of the results was to link the spoke mode to incomplete ionization and to describe its decrease at higher power levels. It was found that rotating spokes appear more often in low voltage discharges. At the end of this century Lomas studied the spoke phenomena in the United States. He linked the electron current in a high-current-density hydrogen Hall accelerator to a rotating spoke [27]. It was also shown that an azimuthal electric field fluctuation was in phase with a density fluctuation. Calculations showed that 20-70% of the $100\,A$ current was carried via this mechanism.

In the 2000s Chesta observed spoke-like instabilities in low-voltage Hall thruster discharges of approximately $80\ldots200V$ [28]. He also used numerical models to solve the complicated dispersion relation and did stability analysis. Like previous physicists he linked the rotating spoke to electronic processes like ionization. Parker 2010 detected a spoke instability with a high-speed camera and connected it to a large decrease in thruster efficiency due to an increase of backstreaming electrons [29]. In the last years McDonald et al. did parameter studies to do further characterization of the spoke instability [30]. They worked out four statements to classify spoke modes. In the following they will be summarized. Testing several different thrusters with respect to spokes allowed to see that physically larger thrusters lead to higher spoke modes. Mode numbers from $m = 1$ up to $m = 6$ are detectable. All spokes rotate in the direction of the $E \times B$-drift. Parameter studies showed that higher spokes modes travel faster under the same conditions. Using higher magnetic field strengths lead to a stronger and more stable appearance of spokes. At higher magnetic field settings, which means an increase in magnetic field strengths due to higher voltage or optimized operating conditions, higher spoke modes become more dominant. The spoke velocity seems to decrease slightly at a higher magnetic field. Especially the spoke velocity is much smaller than the $E \times B$-drift velocity.

A strong azimuthal asymmetry in radiation from the thruster channel was observed with fast camera imaging of the cylindrical Hall thruster ignition during the first $10\,\mu s$. This indicates a spoke-like structure inside the channel during ignition.

5.3. Particle Fluxes to the Walls

Introducing diagnostic modules for particle fluxes to the walls into the PIC code allows to evaluate possible damage of the satellite by the thruster. The used domain includes 240 cells in r-direction and 890 in z. One cell has a length of $\Delta z = 0,5\lambda_{Db} = 3.715\ 10^{-4}$cm and $\Delta r = 10^{-3}$cm. The timestep for the electrons is chosen as $\Delta t = 0,2/\omega_{pe} \approx 1.12\ 10^{-12}$s. Subcycling for ions and neutrals is used. The ions are updated every 400th step. The timestep for the neutrals is 2000 times larger than the one for the electrons.

The first analysis is the backflow to the thruster. This is analyzed in the cells, which are located at the thruster exit $z = 51.2\,$mm outside the thruster in r-direction $r > R_{Thruster} = 9\,$mm. The region is split into three parts in r-direction. The first part is for $9\,$mm $< r < 14\,$mm, the second from $14\,$mm to $19\,$mm and the third region covers the rest of the domain up to $r = 24\,$mm.
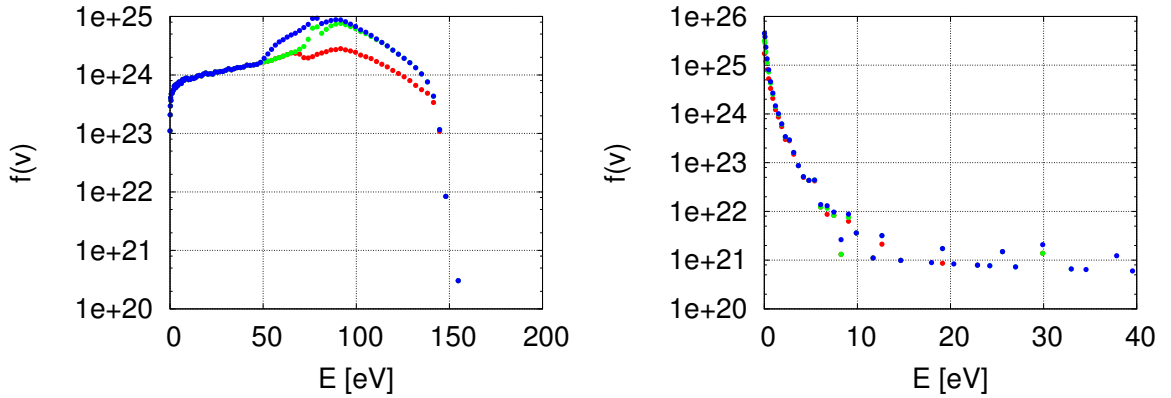

Figure 5.11.: energy distribution for each region of backflowing particles, left ions and right neutrals, red - region 1, green - region 2, blue - region 3

Figure 5.11 shows the number of particles hitting the three regions as a function of their kinetic energy. All regions have a pronounced peak around $80\,$eV. In region 3 there are about ten times more particles than in the other regions. The fastest particles have energies of up to $150\,$eV in region 3. Ions hitting theses surfaces have to make a nearly 180 degree turn from flying outward of the thruster to flying

backwards to the wall. The radius of this half-circle movement is determined by the radial velocity. Higher radial velocities lead to a larger radius and impingement on the wall at larger r.

For the neutrals on the right hand side of Figure 5.11 a significant number of particles is detected in every region, too. Most of them have very small kinetic energies of about only a few eV originating from the thermal source at the anode. The profile of the energy distribution is even more similar in all three regions than for the ions. The higher energies result from charge-exchange with ions. Because the size of the domain is not large enough to cover the whole satellite it is also interesting to detect particles that arrive at the r boundary of the system, which is implemented at grounded metal. The simulation shows that only ions arrive here. The velocity distribution is presented in Figure 5.12
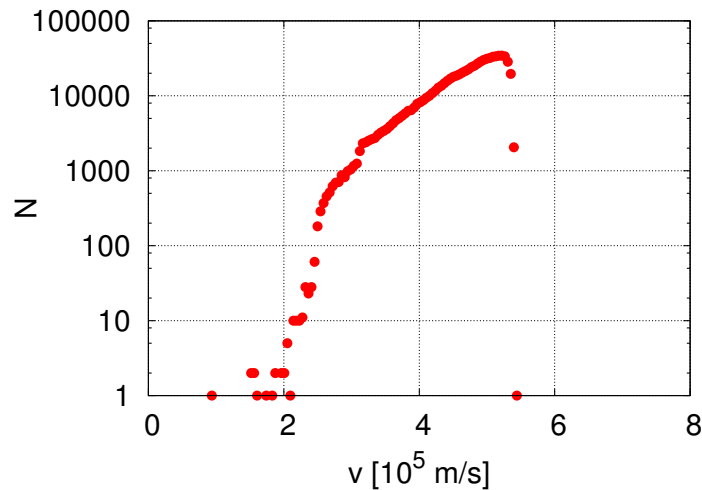
Figure 5.12.: velocity distribution for each region of outflowing ions in r-direction

One can see that ions with velocities between $4700 \, \text{m/s}$ and $2000 \, \text{m/s}$ leave the domain. Most of them are in the high-velocity part of the distribution. These particles are possibly dangerous for the satellite and one should try to extend the domain to understand what happens with them outside the current domain for reliable sputter and lifetime analysis of the satellite. During the simulation the particles hitting each surface region was counted. With these numbers one can derive the particle flux densities. One distinguishes again three regions beginning from the inner part of the domain. Due to rotational symmetry the surface must be calculated as a circular ring with small radius r and larger radius R:

$$A_1 = 2\pi \left((0.014\,\text{m})^2 - (0.009\,\text{m})^2\right) = 3.6128\ 10^{-4}\text{m}^2 \tag{5.3.1}$$

$$A_2 = 2\pi \left((0.019\,\text{m})^2 - (0.014\,\text{m})^2\right) = 5.1836\ 10^{-4}\text{m}^2 \tag{5.3.2}$$

$$A_3 = 2\pi \left((0.024\,\text{m})^2 - (0.019\,\text{m})^2\right) = 6.7544\ 10^{-4}\text{m}^2 \tag{5.3.3}$$

where the i in A_i denotes the region. 10^6 steps with each timestep of $1.1213\ 10^{-12}$s were simulated. The particle flux density is given as:

$$j_1 = 5.5162\ 10^{18}\text{m}^{-2}\text{s}^{-1} \tag{5.3.4}$$

$$j_2 = 6.8989\ 10^{18}\text{m}^{-2}\text{s}^{-1} \tag{5.3.5}$$

$$j_3 = 6.5868\ 10^{18}\text{m}^{-2}\text{s}^{-1} \tag{5.3.6}$$

The same calculation is done for the outflow region. One has to recognize that the surface in this case is a lateral surface area of a cylinder with length $37.8\,\text{mm}$ and radius $24\,\text{mm}$. With this the surface is given as $5.7\ 10^{-3}\text{m}^2$ and the particle flux density can be calculated as

$$j_{out} = 1.252\ 10^{18}\ \text{m}^{-2}\text{s}^{-1} \tag{5.3.7}$$

This is four times smaller than the backflow. Now the goal will be to estimate the sputtering as a function of time to be able to derive a limit for the lifetime of solar panels due to sputtering from ion thruster plumes. Using the SD.Trim.SP code in its dynamical version it is possible to calculate the sputter depth as a function of the fluence. The input for the simulation are the energy distribution functions for the three regions and material constants of the considered material. Solar cells for spacecraft are mainly built from Silicon Dioxide and Gallium Arsenide. Nowadays the industry uses multi-junction cells. Since this work needs only a rough estimate, Silicon Dioxide and Gallium Arsenide are used. The results of the sputter simulation show a linear dependence between sputtering depth and fluence. This can be seen in Figure 5.13. It shows that the sputter coefficient is nearly constant for increasing fluence. Consequently the surface depth resulting from sputtering shows a linear dependency to the fluence.

Therefore, one can easily extrapolate it to longer times. The following depths d in every region are determined for a time of $1000\,\text{h}$ using SiO_2 :
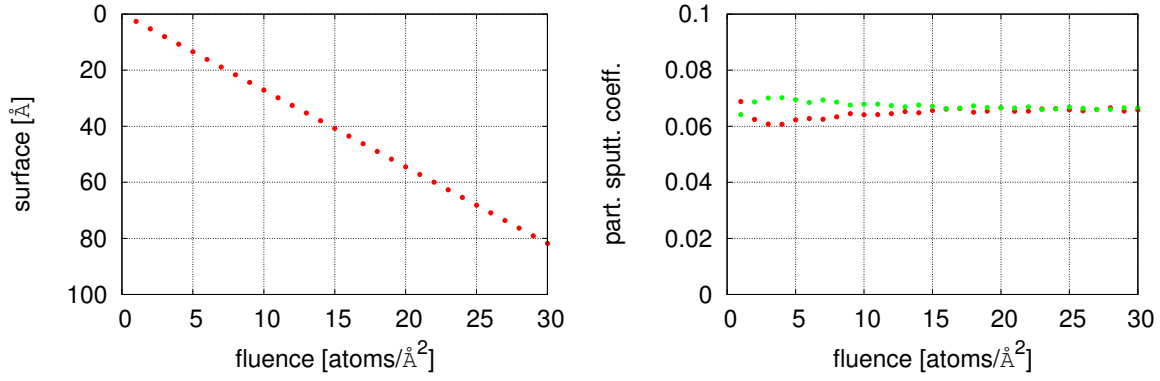
Figure 5.13.: surface depth (left) and sputter coefficients of Ga (right red dots) and As (left green dots) as a function of fluence

$$d_1 = 5.6185\,\mu\text{m} \tag{5.3.8}$$

$$d_2 = 7.8778\,\mu\text{m} \tag{5.3.9}$$

$$d_3 = 6.8766\,\mu\text{m} \tag{5.3.10}$$

For Gallium Arsenide the resulting depths are much larger.

$$d_1 = 54.16\,\mu\text{m} \tag{5.3.11}$$

$$d_2 = 78.11\,\mu\text{m} \tag{5.3.12}$$

$$d_3 = 69.43\,\mu\text{m} \tag{5.3.13}$$

This can be explained by the different characteristics of both materials. GaAs has a much higher atomic mass and larger atomic radii compared to SiO_2. One can imagine that the arriving Xenon atoms are able to penetrate the surface deeper, if the surface consists of light and small particles. This can be seen in the Figure 5.14.

In 5.14 an incoming Xenon beam impinges on a surface, which is built of SiO_2 or GaAs. As expected the penetration depth is larger for SiO_2. For GaAs most the energy of incoming Xenon atoms is assimilated near the surface and particles in this region have a much higher chance to leave the surface as sputtered atoms. This leads to higher sputter rates for GaAs than in SiO_2 where the energy is deposited deeper and only a few atoms leave the material.

Solar panels produced for space have thicknesses about $140\,\mu\text{m}$. As first the sputter
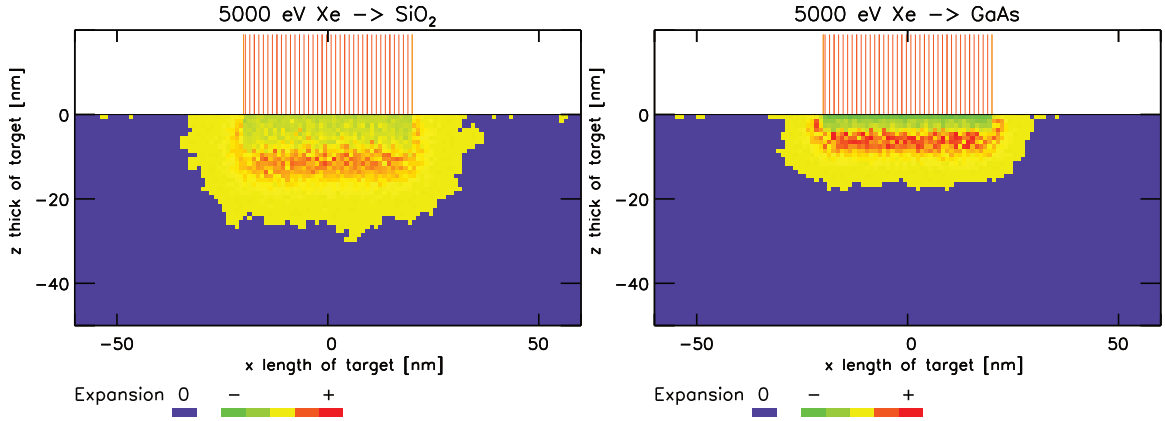
Figure 5.14.: interaction of Xenon particles with a SiO$_2$ surface (left) and with a GaAs surface (right)

depths for SiO$_2$ seem very worrying. But the solar panels are far away from the point where the backflowing particles were analyzed in the simulation. According to [31] the ion density is decreasing by at least three orders of magnitude radially between the center and $r = 1$ m. Therefore the calculated particle flux densities must be corrected by a factor of 1000. This finally results in sputter depths that are far beyond a critical limit after 1000 h. One can possibly get into critical regions for longer times like 100 000 h.

5.4. Domain Extension

In this section the extension of the domain using the newly developed solver is presented. In the upper part of Figure 5.16 the potential calculated with a smaller domain be seen. The size of the domain is 89 mm $\times$ 24 mm. In the lower part of Figure 5.16 the domain is enlarged. Its size is now 127 mm $\times$ 48 mm. Especially in the plume region there are large differences observable between both solutions.

Whereas in the small domain the decrease in potential takes place very fast driven by the boundary condition, the larger domain shows a much smoother decrease.

At the borders of the smaller domain, where $\phi = 0$ V is fixed, the large domain still shows potential values of several Volts. This difference results in stronger electric fields in the smaller domain compared to the larger one. The potential in the larger domain is less influenced by the boundary condition. An even larger domain is expected to resolve the discrepancy of angular ion distributions between modeling and experiment.
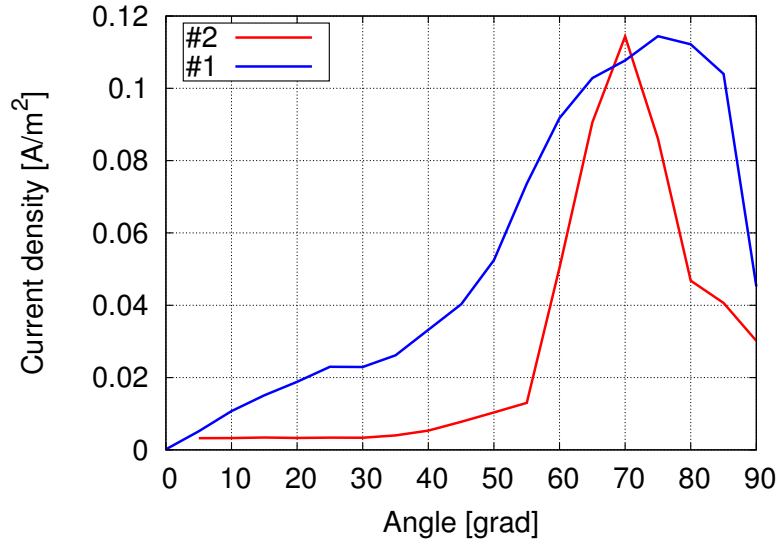
Figure 5.15.: ion angular current distribution function of old [11] (red) and new simulation (blue)

How the domain size affects the angular distribution one can see in Figure 5.15. The experimental result was compared to the older simulation in Figure 3.2 with the smaller domain. The result of the larger domain gets closer to the experimental studies, but it is still far away. One can hope, that with an additional enlargement of the domain this effect increases and one gets even closer to the experiment.

Small domain

Large domain
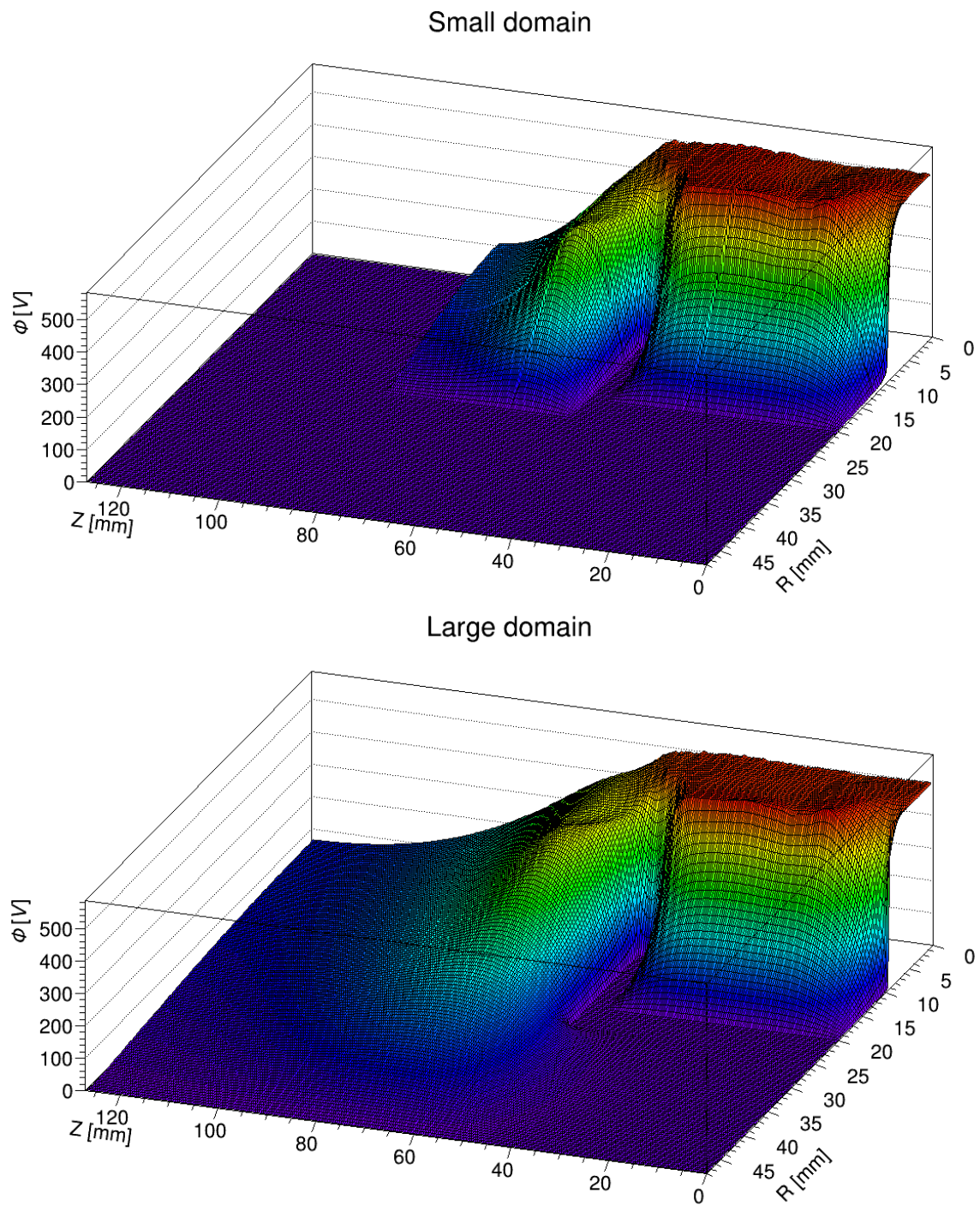
Figure 5.16.: PIC potential solution for different domain sizes

6. Conclusions and Outlook

The goal of the work was to study the physics of the plume of ion thrusters. This was done for the example of the HEMP-T, where its basic operational principles were introduced. To study the plume region, the numerical development of a non-equidistant Poisson solver for PIC applications is needed. Different solver methods were tested with the result that the most promising one is the explicit and exact LU decomposition method with its fast backsolve. This particularly developed Poisson solver was validated with some analytic results for test problems to check the physical correctness of the solver. With the One-Grid Approach it is possible to simulate large two dimensional grids within reasonable times. These grids allow to resolve the whole plume, if one uses a coarsening of grid cells in the plume. The coarsening is physically motivated due to an immense increase of the Debye scale in the plume due to a strong density reduction.

A characterization of the basic physics elements acting in the plume region was done for HEMP-T. For this, diagnostics tools for the PIC code were implemented for velocity distribution functions and domain boundary fluxes. This helped to get a better understanding of the underlying physics in the plume, like the importance of charge-exchange collisions for coupling the ion and neutral dynamics. A sputtering calculation was made to be able to discuss lifetime limits of ion thrusters and their interaction with the satellite.

For future work, it will be interesting to extend the simulated domain even further to reach a fully kinetic model of the interaction of different ion thrusters with the satellite components.

A. Appendix

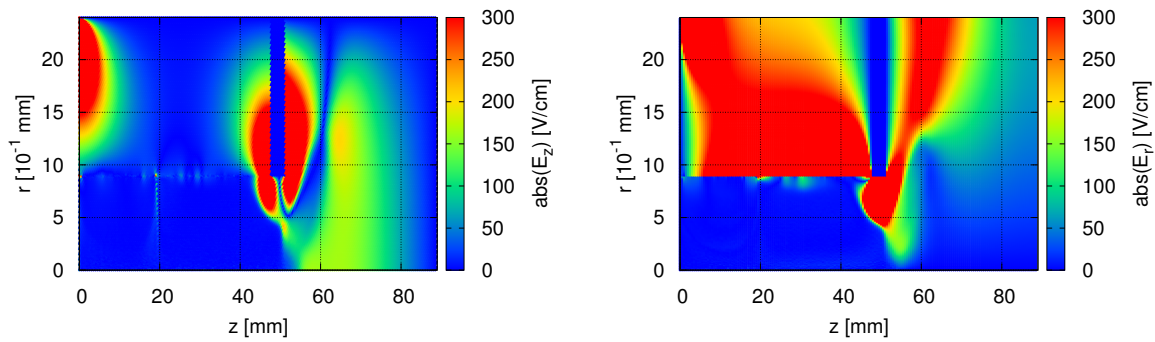## A.1. Additional Results of the HEMP-T Simulation

Figure A.1.: absolute value of the electric field in axial (left) and radial (right) direction over the whole domain
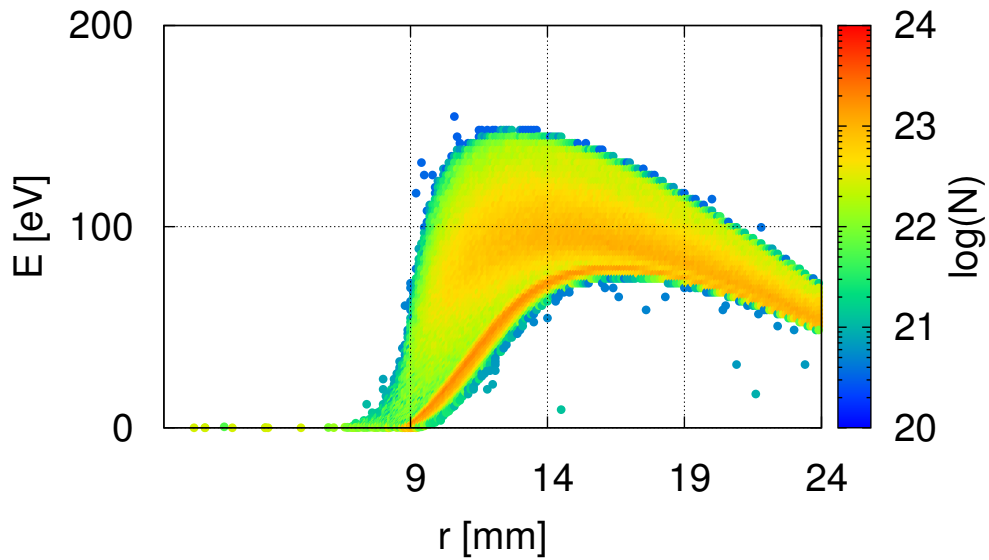

Figure A.2.: number of ions reaching the grounded wall above the thruster exit at $z = 51.2\,\mathrm{mm}$ as a function of the kinetic energy E and the radial position r
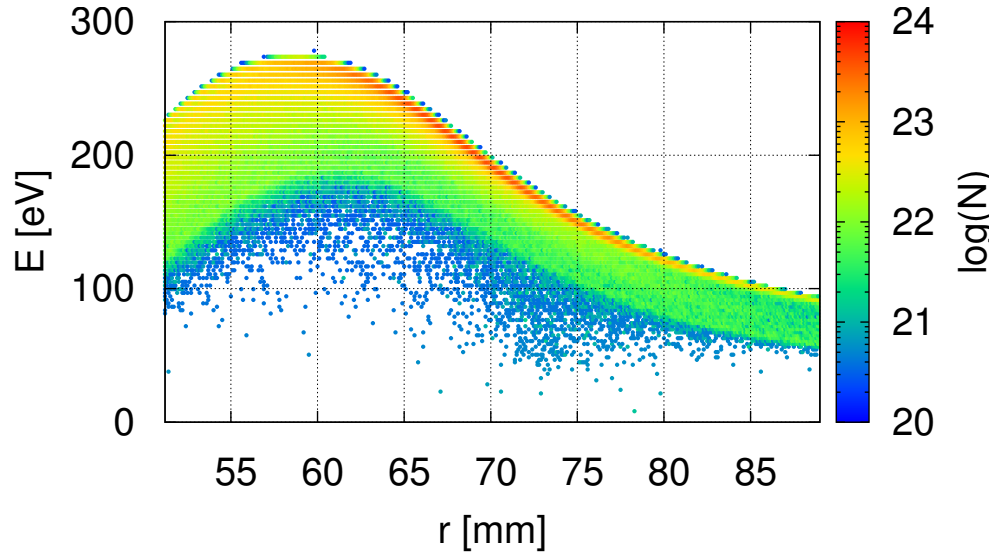
Figure A.3.: number of ions flying outwards the domain in radial direction as a function of the kinetic energy E and axial position z
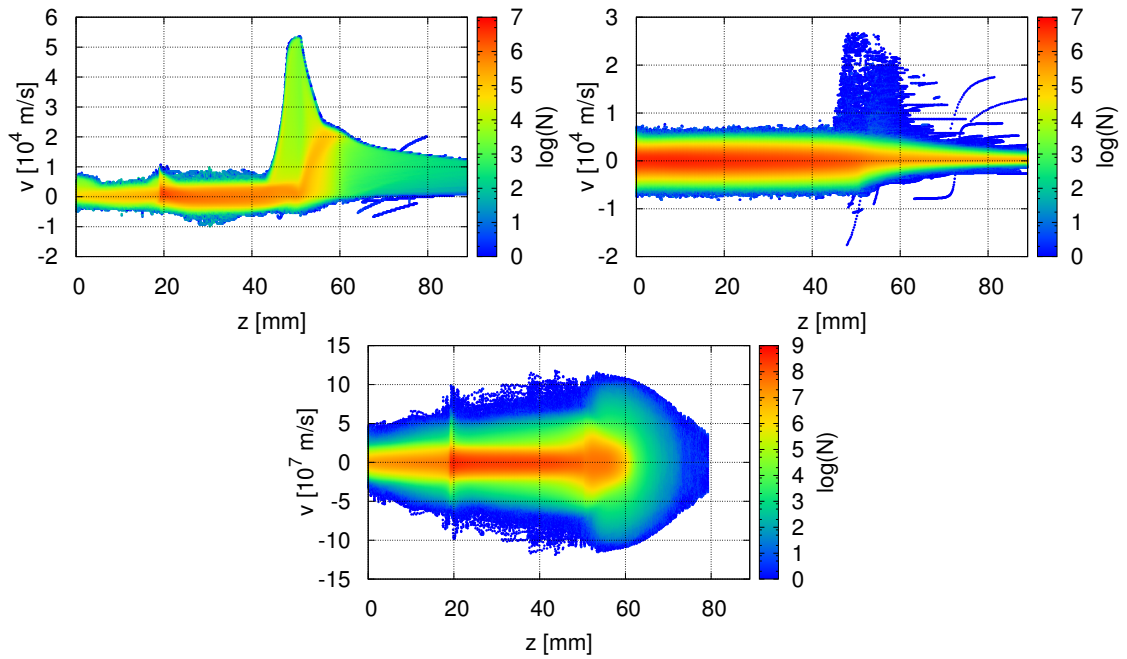

Figure A.4.: distribution of the radial component of the velocity of ions (upper left side), neutrals (upper right side) and electrons (bottom), summed over all particles with $r < R_{thruster}$, ions have a strong peak according to the potential drop to the grounded wall at the exit cusp, neutrals the same due to charge-exchange collisions, electron heating in the cusps is visible
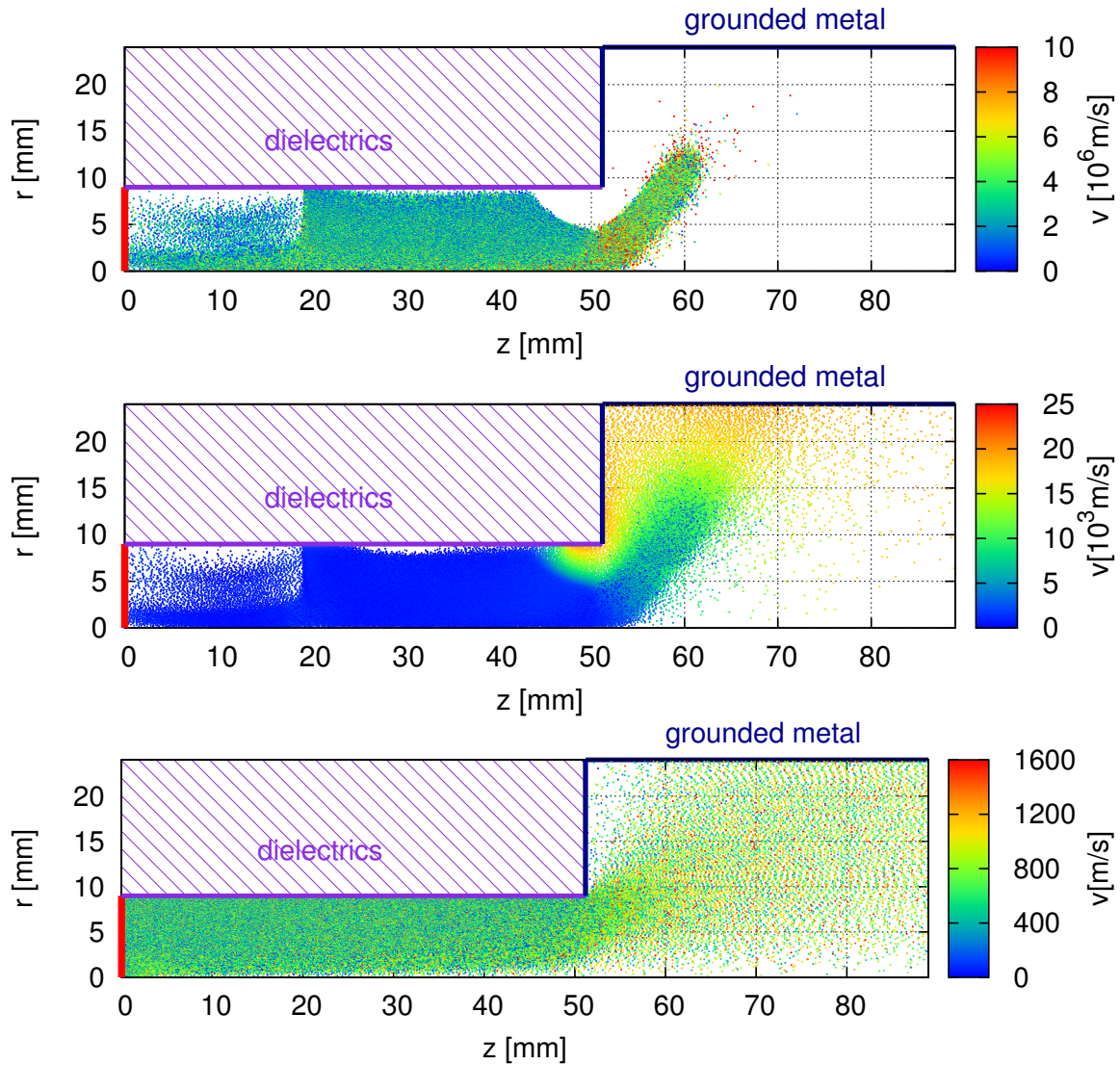
Figure A.5.: scatter plot of the position of every calculated electron (upper plot), ion (middle plot) and neutral (bottom plot) with the color encoded the absolute value of the velocity, due to the cylindrical geometry (cells near the axis are smaller than in the outer part) this does not directly represent the density, however electron trapping and the limited ion wall contact in the cusps is visible

Bibliography

[1] Dan M. Goebel and Ira Katz. *Fundamentals of electric propulsion: ion and Hall thrusters*, volume 1. Wiley, 2008.

[2] N Koch, HP Harmann, and G Kornfeld. Status of the THALES High Efficiency Multi Stage Plasma Thruster Development for HEMP-T 3050 and HEMP-T 30250. In *Proceedings of the 30th International Electric Propulsion Conference*, pages 17–20, 2007.

[3] Ralf Schneider. *Plasma edge physics for tokamaks*. IPP, 2001.

[4] GD Hobbs and JA Wesson. Heat flow through a Langmuir sheath in the presence of electron emission. *Plasma Physics*, 9(1):85, 2002.

[5] Wolfgang Eckstein. Computer Simulation of Ion-Solid Interactions. *Springer Series in Materials Science*, 10, 1991.

[6] W. Eckstein, R. Dohmen, A. Mutzke, and R. Schneider. *SDTrimSP: A Monte-Carlo Code for Calculating Collision Phenomena in Randomized Targets*. Max-Planck-Institut für Plasmaphysik, 2007.

[7] G. Kornfeld, H. Seidel, and J. Wegener. Plasma Accelerator Arrangement, 1999. Priority: Germany No. 198 28 704.6, filed 26 June 1998.

[8] D. Tskhakaya, K. Matyash, R. Schneider, and F. Taccogna. The Particle-In-Cell Method. *Contributions to Plasma Physics*, 47(8-9):563–594, 2007.

[9] S. Patankar. *Numerical heat transfer and fluid flow*. Taylor & Francis, 1980.

[10] Konstantin Matyash, Ralf Schneider, Andreas Mutzke, Oleksandr Kalentev, Francesco Taccogna, Norbert Koch, and Martin Schirra. Self-consistent kinetic simulations of SPT and HEMP thrusters including the near-field plume region. *Bulletin of the American Physical Society*, 54, 2009.

Bibliography

[11] O Kalentev Matyash, R Schneider, F Taccogna, N Koch, and M Schirra. Kinetic simulation of the stationary HEMP thruster including the near-field plume region. *Proceedings of the 31st International Electric Propulsion Conference*, pages 20–24, 2009.

[12] Xiaoye S. Li. An Overview of SuperLU: Algorithms, Implementation, and User Interface. *ACM Transactions on Mathematical Software*, 31(3):302–325, September 2005.

[13] Julia Duras. Instabilities in ion thrusters by plasma-wall interactions. Master's thesis, Ernst-Moritz-Arndt University Greifswald, 2011.

[14] Anthony Nicholls and Barry Honig. A rapid finite difference algorithm, utilizing successive over-relaxation to solve the Poisson–Boltzmann equation. *Journal of computational chemistry*, 12(4):435–445, 1991.

[15] Orion Ciftja, Arica Babineaux, and Nadia Hafeez. The electrostatic potential of a uniformly charged ring. *European Journal of Physics*, 30(3):623, 2009.

[16] Wolfram Research, Inc. functions.wolfram.com. `http://functions.wolfram.com/EllipticIntegrals/EllipticK/20/01/`, april 2013.

[17] N Koch, M Schirra, S Weis, A Lazurenko, B van Reijen, J Haderspeck, A Genovese, P Holtmann, R Schneider, K Matyash, et al. The HEMP-T Concept - A Survey on Theoretical Considerations and Experimental Evidences. *Proceedings of the 32nd International Electric Propulsion Conference*, 2011.

[18] J.A. Bittencourt. *Fundamentals of Plasma Physics*. Springer Verlag, third edition, 2004.

[19] F Taccogna, R Schneider, S Longo, and M Capitelli. Kinetic simulations of a plasma thruster. *Plasma Sources Science and Technology*, 17(2):024003, 2008.

[20] AV Phelps. The application of scattering cross sections to ion flux models in discharge sheaths. *Journal of applied physics*, 76(2):747–753, 1994.

[21] M.R. Carruth and M.E. Brady. Measurement of the charge-exchange plasma flow from an ion thruster. *Journal of Spacecraft and Rockets*, 18(5):457–461, 1981.

[22] Francesco Taccogna, Savino Longo, and Mario Capitelli. Particle-in-cell with Monte Carlo simulation of SPT-100 exhaust plumes. *Journal of spacecraft and rockets*, 39(3):409–419, 2002.

[23] Konstantin Matyash. Kinetic simulation of HEMP thruster including the near-field plume region. Presented at the 31st International Electric Propulsion Conference, Ann Arbor, Michigan, 2009.

[24] K. Matyash, R. Schneider, O. Kalentev, Y. Raitses, and N. J. Fisch. Numerical investigations of a cylindrical Hall thruster. *IEPC-2011-070*, August 2012.

[25] G.S. Janes and R.S. Lowder. Anomalous Electron Diffusion and Ion Acceleration in a Low-Density Plasma. *Physics of Fluids*, 9:1115, 1966.

[26] S Yoshikawa and DJ Rose. Anomalous diffusion of a plasma across a magnetic field. *Physics of Fluids*, 5:334, 1962.

[27] PJ Lomas and JD Kilkenny. Electrothermal instabilities in a Hall accelerator. *Plasma Physics*, 19(4):329, 1977.

[28] Enrico Chesta, Cheryl M. Lam, Nathan B. Meezan, Daniel P. Schmidt, and Mark A. Cappelli. A characterization of plasma fluctuations within a Hall discharge. *Plasma Science, IEEE Transactions on*, 29(4):582–591, 2001.

[29] JB Parker, Y Raitses, and NJ Fisch. Transition in electron transport in a cylindrical Hall thruster. *Applied Physics Letters*, 97(9):091501–091501, 2010.

[30] S McDonald and D Gallimore. Parametric investigation of the rotating spoke instability in Hall thrusters. In *Proceedings of the 32nd International Electric Propulsion Conference*, 2011.

[31] RI Samanta Roy, DE Hastings, and NA Gastonis. Ion-thruster plume modeling for backflow contamination. *Journal of Spacecraft and Rockets*, 33(4):525–534, 1996.

Acknowledgments

At the end of this thesis I want to thank all the people, who helped me during the work for my master thesis and the last 5 years. First of all I want to express my gratitude to my supervisor Prof. Dr. Ralf Schneider for his great support, interesting physics discussions and for the daily hot chocolate. Furthermore, I want to thank the members of the COMPUS group, especially Julia and Sascha for explaining issues of thruster physics.

I am grateful for my girlfriend Karo who understood the occasional necessity of some longer work days. At this point I like to mention that the last 5 years in Greifswald made it possible to meet some great friends. They are and were responsible for some unforgettable days or mostly evenings. I hope for many more of them.

Last but not least I like to thank my parents for their never-ending trust and support during 5 long years of studying.